

DTIC FILE COPY

2

GL-TR-90-0187

**AD-A233 452**

PHOTOMETRIC-PHOTOGRAMMETRIC ANALYSIS OF VIDEO IMAGES  
OF A VENTING OF WATER FROM SPACE SHUTTLE DISCOVERY

I. L. Kofsky  
N. H. Tran  
M. A. Maris  
D. L. A. Rall  
C. A. Trowbridge

PhotoMetrics, Inc.  
4 Arrow Drive  
Woburn, MA 01801-2057

15 June 1990

Scientific Report No. 2

DTIC  
ELECTE  
MAR 21 1991  
S E D

Approved for public release; distribution unlimited.

GEOPHYSICS LABORATORY  
AIR FORCE SYSTEMS COMMAND  
UNITED STATES AIR FORCE  
HANSCOM AFB, MASSACHUSETTS 01731-5000

"This technical report has been reviewed and is approved for publication"

Edmond Murad

EDMOND MURAD  
Contract Manager

E. Murad  
for

CHARLES P. PIKE, Chief  
Spacecraft Interactions Branch

FOR THE COMMANDER

William Swider

WILLIAM SWIDER, Deputy Director  
Space Physics Division

This report has been reviewed by the ESD Public Affairs Office (PA) and is releasable to the National Technical Information Service (NTIS)

Qualified requestors may obtain additional copies from the Defense Technical Information Center. All others should apply to the National Technical Information Service.

If your address has changed, or if you wish to be removed from the mailing list, or if the addressee is no longer employed by your organization, please notify GL/IMA, Hanscom AFB, MA, 01731. This will assist us in maintaining a current mailing list.

Do not return copies of this report unless contractual obligations or notices on a specific document requires that it be returned.

UNCLASSIFIED

SECURITY CLASSIFICATION OF THIS PAGE

REPORT DOCUMENTATION PAGE				
1a REPORT SECURITY CLASSIFICATION Unclassified			1b RESTRICTIVE MARKINGS None	
2a SECURITY CLASSIFICATION AUTHORITY N/A			3 DISTRIBUTION/AVAILABILITY OF REPORT Approved for public release; Distribution unlimited.	
2b DECLASSIFICATION/DOWNGRADING SCHEDULE N/A				
4 PERFORMING ORGANIZATION REPORT NUMBER(S)  PhM-P-08-90			5. MONITORING ORGANIZATION REPORT NUMBER(S)  GL-TR-90-0187	
6a NAME OF PERFORMING ORGANIZATION  PhotoMetrics, Inc.		6b OFFICE SYMBOL (If applicable)		7a. NAME OF MONITORING ORGANIZATION  Geophysics Laboratory
6c ADDRESS (City, State, and ZIP Code)  4 Arrow Dr. Woburn, MA 01801-2057			7b. ADDRESS (City, State, and ZIP Code)  Hanscom AFB, MA 01731-5000	
8a. NAME OF FUNDING, SPONSORING ORGANIZATION		8b. OFFICE SYMBOL (If applicable)		9. PROCUREMENT INSTRUMENT IDENTIFICATION NUMBER  F19628-88-C-0070
8c. ADDRESS (City, State, and ZIP Code)			10 SOURCE OF FUNDING NUMBERS	
			PROGRAM ELEMENT NO. 63220	PROJECT NO. S321
			TASK NO. 31	WORK UNIT AA
11 TITLE (Include Security Classification)  Photometric-Photogrammetric Analysis of Video Images of a Venting of Water from Space Shuttle Discovery.				
12 PERSONAL AUTHOR(S) I. L. Kofsky, N. H. Tran, M. A. Maris, D. L. A. Rall, C. A. Trowbridge				
13a TYPE OF REPORT Scientific Report #2		13b TIME COVERED FROM 890531 TO 900531		14. DATE OF REPORT (Year, Month, Day) 90/06/15
15. PAGE COUNT 86				
16 SUPPLEMENTARY NOTATION				
17 COSAT CODES			18. SUBJECT TERMS (Continue on reverse if necessary and identify by block number)  Spacecraft contamination      Water ventings Particulate Scattering      Video photometry	
FIELD	GROUP	SUB-GROUP		
19 ABSTRACT (Continue on reverse if necessary and identify by block number)  The patterns of scattering of visible sunlight by the ice particles that formed from fuel cell-product water vented just before dawn into the wake of Shuttle Orbiter are photometrically reduced and analyzed. This initially coherent heated liquid stream is found to break up within ~1 m from the nozzle into irregular polydisperse drops of mean size comparable with its initial 1½ - µm diameter (much as was observed in laboratory simulations), which are accompanied by a much less-dense cloud of submicron ice droplets produced when the evaporated/sublimed water gas overexpands and partially recondenses. The discrete large drops dominate the images of the backlit trail taken by intensified-video cameras onboard the spacecraft, while the radiance from the efficiently-scattering small particles is responsible for virtually all of the signal at a long-focus (½°-field) camera precisely tracked on the spacecraft from the Air Force Maui (mountaintop)				
20 DISTRIBUTION/AVAILABILITY OF ABSTRACT <input type="checkbox"/> UNCLASSIFIED/UNLIMITED <input type="checkbox"/> SAME AS RPT <input type="checkbox"/> DTIC USERS			21. ABSTRACT SECURITY CLASSIFICATION Unclassified	
22a. NAME OF RESPONSIBLE INDIVIDUAL Edmond Murad			22b TELEPHONE (Include Area Code) 617/377-3176	22c. OFFICE SYMBOL GL/PHK

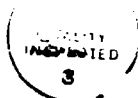
UNCLASSIFIED

SECURITY CLASSIFICATION OF THIS PAGE

## 19. ABSTRACT (continued)

Optical Station. We calculated the mean radius of these smaller ice particles along the  $\sim 2\frac{1}{2}$  km of detectable trail from the video photocurrent distribution and their radiative-evaporative energy balance in the low-earth orbital environment, finding that application of a small correction for surface roughening (such as was seen in laboratory experiments) would fit the sublimation rates. The small ice particles transition from geometric (Mie) to Rayleigh scattering over this trajectory (relative to the spacecraft); in contrast the large particles lose only a very small fraction of their mass. The irradiances from individual ice drops measured from onboard, and the radiances of the trail measured from the ground, with the thermodynamically-predicted solid and gas fractionation, constrain the mean diameter of the large particles and fraction of the vented water volume recondensed into the small particles.

Accession For	
NTIS GRA&I	<input checked="" type="checkbox"/>
DTIC TAB	<input type="checkbox"/>
Unannounced	<input type="checkbox"/>
Justification	
By	
Distribution/	
Availability Codes	
Dist	Avail and/or Special
A-1	



UNCLASSIFIED

SECURITY CLASSIFICATION OF THIS PAGE

## FOREWORD

This report documents the principal task performed by PhotoMetrics in optical sensing of spacecraft environments during the second of three scheduled years of Contract F19628-88-C-0070 with the Spacecraft Interactions Branch (PHK) of Geophysics Laboratory, Air Force Space Technology Command. The report of the first year's work, covering principally the further topics hydroxyl electronic-band radiations excited by interactions of control rocket engine exhaust and photolysis of outgassed water vapor, spectroscopy of particulate contaminants, and planning of radiometry in space experiments, is Reference 15. Previous work by PhotoMetrics on related optical contamination and foregrounds issues, with a focus on spacecraft-induced glows and excitative reactions of high kinetic energy exhaust gases with the orbital atmosphere, is reported in Reference 14.

The research reported here is a complete reduction, analysis, and interpretation of low-light-level video data on a venting of sunlit excess water into the wake of Shuttle Orbiter, from an experiment planned and executed by Geophysics Laboratory in March 1989. Our findings about the sizes and spatial distribution of the ice particles that quickly form from the liquid stream apply in assessing the foregrounds and backgrounds presented to spaceborne surveillance sensors by water dumps, as well as in the disciplines listed on page 1. Some estimates of the radiant intensities at infrared wavelengths (not measured in the experiment reported) appear in Appendix D. The results of this analysis are now being applied in planning active probing of the two-component ice particle trail, using powerful lidars.

We communicated a preliminary version of some of these results in a (refereed) Geophysical Research Letter (Ref 20), and have prepared a presentation for a forthcoming USAF-NASA symposium on spacecraft environments (Ref 21). This full report is now being put into the appropriate format for publication in a technical journal. The large number of co-authors in these references acknowledges the contributions of GL experiment design and management staff who conceived the idea of imaging the sunlight-

scattering distributions against the dark pre-dawn atmosphere with the powerful tracked telescopes at the Air Force Maui (HI) Optical Station; the operators of the video cameras at both AMOS and onboard Shuttle Orbiter "Discovery"; and the organization that provided information about the thermodynamics of water in the near vacuum low earth orbital environment. (Some further acknowledgements appear in Ref 20). The actual writing of Ref 20 was the responsibility of PhotoMetrics and GL/PHK, and of Ref 21, PhotoMetrics. Dr. N. H. Tran merits particular credit for the physical interpretation of the discontinuous slope of the axial radiance of the wake trail (Figure 5), as due to transitioning of the radii of the visible sunlight-scattering, subliming ice particles from the "geometric" into the Rayleigh regime.

- - - - -

Other projects (which are to be documented in the Final Contract Report) included a similar photometric-photogrammetric analysis and interpretation of images of the luminosity excited by rocket combustion-product gases exhausted at a series of angles to the orbital trajectory direction (on shuttle missions STS-29 and -33), which included preparation of a major fraction of a technical paper that is to be submitted for journal publication; calculation of the spectral distribution of the visible and infrared radiation from these exhaust interactions (following identification of the excitation mechanism), and application of the emission intensity pattern to space surveillance/tracking; specification of measurements of the optical signal from earth-orbiting (space) debris; and continuation of planning of ground- and space vehicle-borne sensing, both active and passive, for space experiments.

Mrs. Natalie Bennett undertook full responsibility for typing this manuscript, and D. J. Kenny, D. P. Villanucci, and R. B. Sluder provided valuable assistance in preparing the figures. The authors gratefully acknowledge the continuing support, coordination, and encouragement of E. Murad (CTM), C. P. Pike, and their colleagues of GL's Spacecraft Interactions Branch.

## TABLE OF CONTENTS

	<u>PAGE</u>
FOREWORD	iii
TABLE OF CONTENTS	v
LIST OF ILLUSTRATIONS	vii
LIST OF TABLES	viii

### SECTION

1. Introduction	1
2. Overview of the Experiment	4
3. Predicted Behavior of the Vented Water	7
3.1 Millimeter-Diameter Particles	7
3.2 Submicron Particles	9
3.3 Spatial Distributions of the Ice Particles	10
4. Stationarity of the Water Dump	11
5. Telescope-Camera	13
5.1 Specifications	13
5.2 Photometry	14
5.3 Overview of the Ground Images	16
6. Onboard Cameras	17
6.1 General	17
6.2 Photometry and Photogrammetry	21
6.3 Overview of the Onboard Images	24
6.3.1 Cabin Camera	25
6.3.2 Tail Camera	25
6.3.3 Outboard Camera	28
7. Velocity of the Large Ice Particles	29
8. Photometric Analysis of the AMOS Visible Images	31
9. Absolute Brightnesses of the Submicron-Particle Cloud	35
10. Photometric Analysis of the Onboard-Camera Images	40
11. Particle Parameters	42
12. Radiation and Scattering at Other Wavelengths	44
13. Contamination of Orbiter	44
14. Conclusions	45

# TABLE OF CONTENTS (concluded)

<u>SECTION</u>	<u>PAGE</u>
Appendix A    SUBLIMATION FROM SUBMICRON-DIAMETER ICE PARTICLES IN THE LOW EARTH-ORBITAL ENVIRONMENT	49
Theoretical Background	49
Particle Radius Calculations	52
Calculations of the Trail Radiance	53
Surface Roughening	54
Conclusions	56
Appendix B    TEMPERATURE HISTORY OF THE SUBMICRON ICE PARTICLES	58
Background	58
Calculation	60
Appendix C    TEMPERATURE HISTORY OF THE MILLIMETER-DIAMETER ICE PARTICLES	65
Introduction and Background	65
Qualitative Cooling Issues	66
Energy Balance	68
Conclusion	70
Appendix D    INFRARED RADIATION FROM THE WATER TRAIL	73
Scope	73
Discussion	73
REFERENCES	77



# LIST OF ILLUSTRATIONS

<u>FIGURE</u>		<u>PAGE</u>
1	Views of the water/ice particle trail from the two cameras onboard Discovery, and in the space-tank experiments of Ref 7.	2
2.	Montage of six video images of the trail from the AMOS telescope.	3
3.	Solar scatter angle $\eta_1$ , aspect angle to trail axis $\eta_2$ , zenith angle of Orbiter and trail $\eta_3$ , slant range, and schematic of the viewing geometry from AMOS.	6
4.	Equi-photocurrent contour plot of the groundbased image of the trail at $61^\circ$ zenith, $71^\circ$ azimuth.	18
5.	Axial and transverse-summed relative radiances of the trail in Figure 4.	19
6.	Relative visible radiances along lines transverse to the long axis of the trail in Figure 4.	20
7.	Views of the backlit trail from Discovery's aft video camera at three plate scales and pointing azimuths.	22
8.	Digitized image frame from the aft video camera, and a brightness profile across the trail at $\sim 26$ m from the venting nozzle.	23
9.	Photometric scattering functions of $0.2 \mu\text{m}$ , $2 \mu\text{m}$ , and $20 \mu\text{m}$ radius ice particles at $0.55 \mu\text{m}$ , with the Mie oscillations suppressed.	27
10.	Calculated absolute axial radiances of the clouds of submicron-and $\sim$ mm-diameter particles in the projection to AMOS of Figure 4.	38
11.	Small particle abundance-large particle size diagram of the water trail.	43
A1.	Emissivity of large and small spherical ice particles calculated from the complex index of refraction at 266K.	51

# LIST OF ILLUSTRATIONS (concluded)

<u>FIGURE</u>	<u>PAGE</u>
B1. Vapor pressure and heat of vaporization of water.	59
B2. Temperature history of the submicron ice particles.	62
B3. Graphical solution to equilibrium temperature of the small and large ice particles.	63
C1. Surface temperature history of the assumed-spherical $\sim$ mm ice particles.	71

## LIST OF TABLES

<u>TABLE</u>	<u>PAGE</u>
1. Summary of Results from the Analysis of the Ice Particle Trail Images.	46
D1. Radiation from the Water Trail at Other than Visible Wavelengths.	74
D2. Intrared Radiances of Thermal Emission Viewing Perpendicular to the Trail Axis.	74

## 1. Introduction

We reduce and interpret here the patterns of scattering of visible sunlight by the ice particles that formed from supply water vented through a narrow orifice into the wake of Orbiter "Discovery" (STS-29, Orbit 49) on 16 March 1989. The data set consists of intensified-video images from both onboard (the first that have been made available) and a high-altitude ground station (to our knowledge, the only such photographs of the release of material from space shuttle operations). Typical views of the water trail in these projections are reproduced in Figures 1 and 2, and further images from the most favorably located of the three onboard cameras are in Figure 7.

These visible-light distributions provide information about the phenomenology of water dumps in the low earth-orbital environment from which the radiances at other wavelengths can be determined--infrared being of principal interest (see Appendix D) --, to assess the effectiveness of releasing high vapor pressure liquids to alter the signatures of satellites and re-entry bodies. The findings about the droplet sizes, spatial distributions, and velocities, and the portioning of water into its solid and gas phases, also apply to several issues in space physics and operations. These include foregrounds in optical astronomy and remote sensing of the atmosphere (as well as in surveillance); lifetimes of earth-orbiting debris, and the energy balance of comets and meteors near the earth; interaction of outgassed water vapor (Ref 1) and the spacecraft itself (Ref 2) with the ionosphere; F-region plasma depletion (through accelerated recombination of molecular ions; see Ref 3); applications of liquid streams in space (for example for cooling and material transport; see Ref 4); and contamination of the outer surfaces of space vehicles by recontact of ejected material (see for example Ref 5, which considers part of the data set analyzed here).

Figure 1. Views of the sunlit

water/ice particle trail from onboard Discovery (a and b) and in the space-simulation chamber of Ref 7 (Figure 8) (c).

a) is a projection to crew cabin window W1, in which the illuminated window edge and reflections from features inside the cabin can be seen. The nozzle is about 5 m from the nearest segment of beam that shows through the window. The decrease in mean exposure with distance outward is probably due to the

$(1/\text{distance})^2$  decrease in irradiance from the macro-particles, as the solar-scatter angle changes only slowly with this distance.

c), in which the scale at the particle stream is about 1/10, appears qualitatively similar to the relatively close-in projection a). b) is a typical view from the zoom camera mounted just forward of Discovery's vertical stabilizer, 17 m behind the venting nozzle. This camera also views to within ~5 m from the origin of the stream. The decrease in brightness of the trail near the vehicle is due to shadowing of direct sunlight by Discovery's body; and the bright area near the center of the frame is most probably the "rainbow" maximum in differential scattering cross section near 135° solar angle (Figure 9).

Further views of the sunlit trail from the bay camera are in Figure 7.

a)

b)

c)

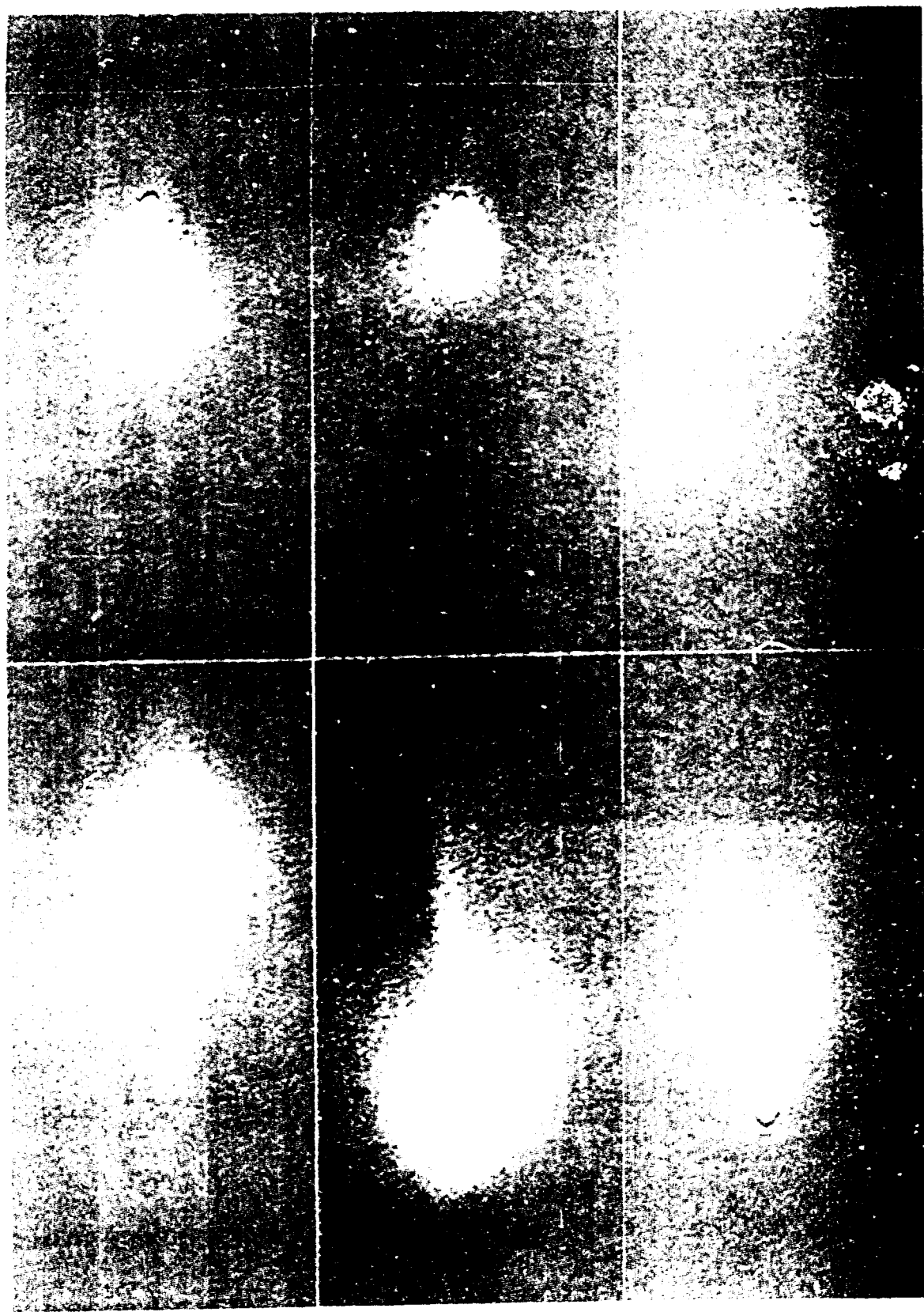


Figure 2. Views of the trail from the  $0.40^\circ \times 0.30^\circ$ -field AMOS telescope.

- a) 15:22:19, zenith angle  $\eta_3$   $5.4^\circ$ , range 331 km. b) 15:22:23 (culmination),  $1.5^\circ$ , 330 km, Orbiter visual magnitude  $-0.2$ .
- c) 15:23:40, (Fig's 4, 5, 6),  $61^\circ$ , 637 km, magnitude  $+3.6$ .
- d) 15:24:20,  $72^\circ$ , 891 km. e) 15:25:40,  $83^\circ$ , 1432 km, magnitude  $+5.6$ .
- f) 15:26:00,  $85^\circ$ , 1570 km. The gain setting is in general different among images. The solar-scattering and aspect angles  $\eta_1$  and  $\eta_2$  are in Figure 3.

## 2. Overview of the Experiment

Relatively pure and gas-free fuel cell product water was forced out into a retrograde orbit through a smooth 60°-halfangle truncated-cone nozzle with 1.4-mm (0.056-inch) diameter opening, at a constant rate of 19.4 g/s. (The supporting data here on Orbiter's trajectory/aspect and system for routinely dumping excess water come from standard NASA sources.) The nozzle was electrically heated to prevent its being blocked by icing (as had occurred in previous spacecraft missions), which resulted in an estimated 60-70°C initial temperature of the water stream. The initial flow direction was antiparallel to the trajectory within <~3° spacecraft's wake.

Discovery was oriented with its long axis pitched 111° down from the horizontal--its open bay facing the nadir hemisphere and earth limb--and starboard wing toward the flight direction. The venting nozzle is on the port side about 3 m below (on the vehicle; above in this flight orientation) and aft of crew cabin window W1, through which a silicon intensifier target (SIT) video camera was manually pointed. (Figure 1 of Ref 2 locates the openings through which supply and waste water are dumped, at  $x = 620.0$ ,  $y = -105.0$ ,  $z = 342.6$  inches in space shuttle system station coordinates.) A second closed circuit TV zoom camera mounted in the cargo bay just forward of the vertical stabilizer and 17 m aft of the nozzle provided another projection of the sunlit water cloud against the dark sky (Figure 1b) about perpendicular to the more restricted views from the cabin (Figure 1a). In addition, a video camera on Orbiter's Remote Manipulator Arm positioned a few m outboard returned corroborating low-contrast images of the early stages of similar daytime ventings of excess water (generally unsuitable for reproduction; described in Section 6.4.3).

Geophysics Laboratory staff planned the water dump to be directly illuminated by the sun while the lower atmosphere above the groundbased telescope-camera remained in the hard earth's shadow. Discovery was at 329 km altitude in a generally

southwest-to-northeast circular orbit, which passed almost directly over USAF's AMOS (Air Force Maui Optical Station) observatory atop Mt. Haleakala, Hawaii ( $21^{\circ}\text{N}$  -  $204^{\circ}\text{E}$ , 3.0 km altitude) a few min before dawn. The spacecraft came into sunlight at  $28.3^{\circ}$  zenith angle and  $245.7^{\circ}$  azimuth at 15:21:59 UT (04:58 local time at AMOS), when the solar depression at its nadir was  $19^{\circ}$ . It was accurately tracked from its trajectory elements by an intensified silicon intensifier target (ISIT) focal plane video camera with 55-cm diameter objective lens (nominal  $f/4$ ) and  $0.4^{\circ} \times 0.3^{\circ}$  field of view. The critical viewing angles and the range to the particle cloud from AMOS are plotted in Figure 3.

The shadow height below Discovery's trajectory decreased to about 120 km when the zenith angle of the trail increased to  $67^{\circ}$  some 2 min later. When direct illumination from the solar disk is limited to these high altitudes, nightglow chemiluminescence and celestial sources (rather than sunlight scattered by the atmosphere) are the principal optical background at the wavelengths to which the AMOS video system responds; as we will find, this radiance is below the camera's noise threshold. Very few discrete ground lights appear in the aft onboard camera's views into the nadir hemisphere, as would be expected from Discovery's trajectory over the Pacific Ocean, and stars are not identifiable in the cabin camera's low elevation-angle images. In contrast, stars with visual magnitude down to about 12 can be seen moving across the narrow field of the large-aperture (and thus high irradiance sensitivity) groundbased camera.

From these ground photographs, we have derived the mean diameters and sublimation rates of the submicron ice particles formed by the two-step process described in Section 3.1. From the photometry and photogrammetry of the onboard images, we have been able to estimate (in Section 11) the fraction of the vented water in these smaller droplets and the mean diameters of the very much larger ice/snow particles that almost immediately form from the liquid.

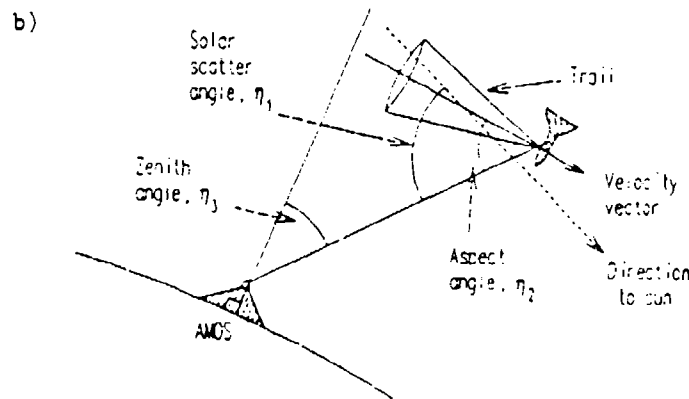
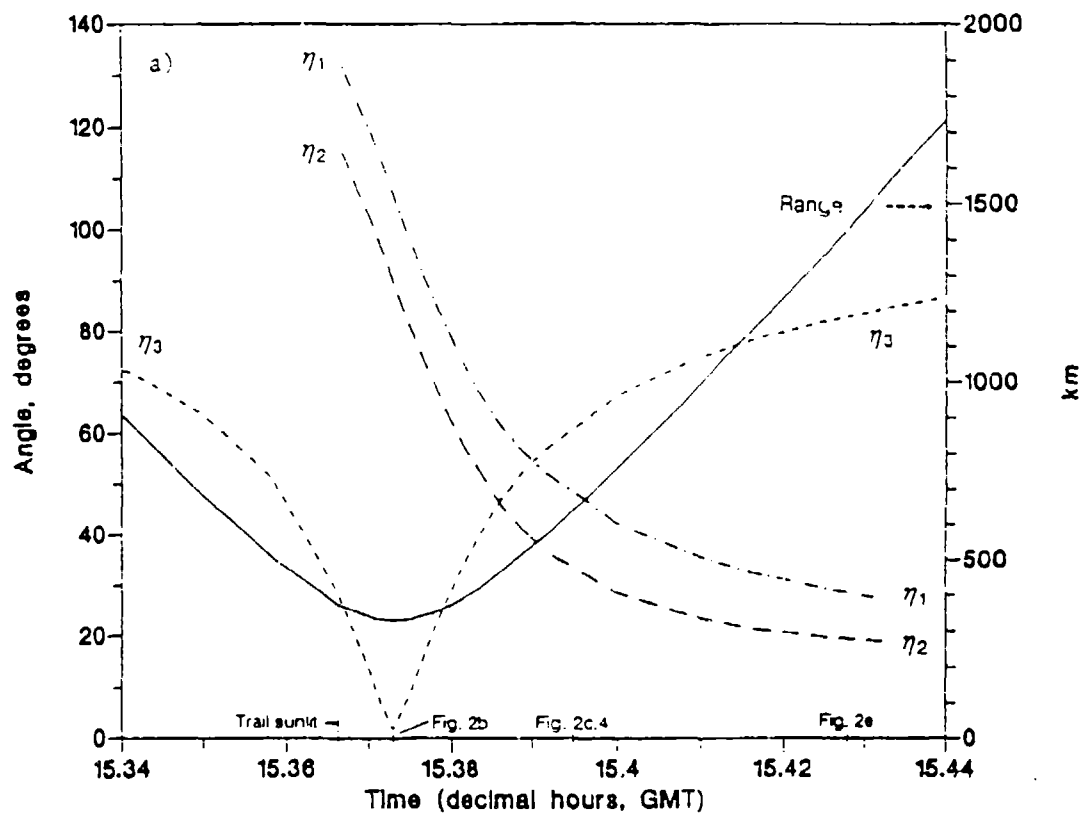


Figure 3. a) Solar scatter angle  $\eta_1$ , aspect angle to trail axis  $\eta_2$ , zenith angle of Orbiter and trail  $\eta_3$ , and slant range to Orbiter from AMOS (solid line) during the water venting. b) Schematic of viewing geometry.



### 3. Predicted Behavior of the Vented Water

Guidance for interpreting the images is provided by recent laboratory simulation experiments in which water streams with about the same initial diameter and flow rate were fired into large vacuum chambers (Ref's 6-9, which reference earlier efforts), and by theory (recently summarized in Ref 4). Millimeters-radius such water columns with typical bulk velocities near 20 m/s were seen to behave as follows.

As the high vapor-pressure liquid quasicylinder enters near-vacuum its outermost layers become cooled by the very rapid evaporation from its surface, while the low heat transfer rate maintains the water near its axis at close to its initial injection temperature. This inner volume is superheated, that is, the vapor pressure exceeds the external pressure (from the gas molecules previously evaporated) plus the surface-tension pressure of the liquid. "Steam" bubbles, nucleated more or less randomly--homogeneously, or by impurities--and dissolved gas thus expand rapidly within the coherent thin stream, tearing it apart (much as water boiling in a pot heated from below spatters).

#### 3.1 Millimeter-Diameter Particles

The water-ice droplets produced in this "flash evaporation" were found in the laboratory experiments to have typical dimensions comparable with the initial diameter of the stream, as would be expected from a cavitation (or for that matter chemical) explosion. In one experiment (Ref 6) they were found to take on "bowl or "dish" shapes, which was interpreted as due to cracking of their less-dense ice outer surfaces by the higher pressure of the unfrozen water inside; that is, the particles photographed were thought to be fragments of larger particles that fractured as successive shells near their surface froze due to the heat loss by sublimation from the immediate surface. The measured halfwidth of the distribution of maximum particle dimensions in this experiment was about twice the nozzle diameter, and in fact most of the volume was in the largest

individual ice particles. We observed a similarly broad spread in sizes in the onboard video images of the essentially-backlit large particles, as discussed in Section 6.3.

These irregular droplets freeze completely by evaporation and sublimation (the larger ones would experience further explosive boiling, or breakup by cracking), becoming somewhat smaller ice particles within seconds. (Estimates of their decrease in surface temperature and dependence of their mean radius on time appear in Appendixes B and C.) The cavitation breakup takes place within  $<1$  m from the venting nozzle when the initial stream diameter is  $>\sim 4$  mm; narrower, cold, pure water columns can propagate stably (Ref 4), while warm, contaminated streams tend to rupture very near the nozzle (Ref 7). (Dissolved foreign gases quickly expand, and steam bubbles form at inhomogeneous-nucleation centers.) Since the heat of vaporization of water is large compared with the sum of its heat of fusion and the heat liberated when the liquid is cooled to its freezing temperature in near-vacuum, most of the vented water appears as these explosion droplets. Straightforward thermodynamic arguments (Ref 3) place the fraction in  $0^\circ\text{C}$  ice at  $4/5$  when the initial temperature of the liquid is near  $70^\circ\text{C}$ ; as these large ice particles continue to sublime (at the rates calculated in Appendixes B and C), the fraction falls to  $3/4$  within the few seconds during which the asymptotic bulk temperature of  $\sim 185\text{K}$  is approached (see Figure C1).

Existing theory does not explicitly predict the transverse velocities imparted to these droplets by the boiling-fracturing(s). However the halfwidth of the angular distributions observed in the laboratory simulations (Ref 7; see Figure 1c),  $\sim 1/4$  radian, provides a measure of this mean radial speed relative to the longitudinal flow speed. This small angle also indicates that the initial venting is the source of most of the kinetic energy of the discrete particles. As these water droplets freeze and cool further they lose mass by sublimation at progressively lower rates, with the result that their scattering

cross-sections change very little as they transit the several-km field of view of the AMOS camera; thus the total surface brightnesses of the ensemble at a fixed sunlight-scattering angle would depend only on the geometric divergence of the beam (which determines the number of particles per  $\text{cm}^2$ -column in the camera's view directions).

### 3.2 Submicron Particles

A more vexed theoretical issue, largely because of the daunting transport geometry and ill-defined distribution of initial diameters and transverse speeds of these explosion-product droplets, is the solid/gas fraction of those water molecules that have evaporated from the short-lived coherent quasicylinder and the droplet cloud. As the molecular mean free paths in the vapor within a few typical-stream diameters are much less than this diameter (as was measured in Ref 7), and (a fortiori) are small compared with the transverse extent of the cloud of droplets produced when the stream bursts, the initial expansion of this vapor is collisional. The gas then cools it expands further radially, and when it becomes supersaturated partially recondenses into ice particles.

Such particles, with diameters near  $0.3 \mu\text{m}$  (and a relatively monodisperse size distribution, reminiscent of that found in fog formed by adiabatic expansion of water vapor--for example in the cloud chambers used in nuclear physics experiments), were identified by light scattering in the tank experiments of Ref's 8 and 9. (Their formation had been predicted in Ref 7.) The fraction of the initially-vented water molecules condensed into these small particles would vary with the diameter, temperature, and concentrations of dissolved gases in the stream, all of which play a part in the rates at which water vaporizes. The estimate for the conditions of Ref 9 is "less than 3%", which represents less than about 1/7 of the flash-vaporized water molecules.

### 3.3 Spatial Distributions of the Ice Particles

A model of the concentrations of these recondensation particles would involve the trajectories of the initial explosion particles, which being formed very soon after the liquid stream is vented and having relatively large total exposed-surface area would be the source of much of the gaseous water. Indeed, as Appendix C indicates, in Discovery's venting only a fraction of this vapor originates from the bundled stream; thus even taking into account the high pressures that result from the high initial water temperature (see Figure B1)--that is, the large local densities of water molecules--the cylindrically-expanding gas from the stream would account for only part of the recondensation-droplets cloud. The mean directed velocity of expanding gas evaporated/sublimed from each drop is the same as that of the drop itself; and, as we show in Section 7, the mean longitudinal velocity of these large drops differs little (if at all) from the initial velocity of the coherent stream. Since the submicron particles by definition form where the water vapor is collisional rather than supersonic--that is, where the gas velocities are randomized in a reference frame of the drop(s)--the transverse velocities of these smaller ice particles [originating from the large particles] would be the same as the transverse velocities of the large particles.

We identify no physical process that imparts a directed longitudinal velocity to the small particles relative to the large particles. Furthermore, the photographs from onboard the spacecraft do not show any evidence of an unresolved sunlight-scattering volume with an angular spread different from that of the cloud of readily-distinguishable, polydisperse, outward-flowing large ice drops. (We return to this important point in our later analysis of the video images.) A related observation confirming that the mean velocities of the two components are sensibly the same is that the angular extent of the large-particle beam (Figure 1a and b, and Figure 7) and the cloud of what we will later show to be submicron particles in the

groundbased-telescope images (Figures 2 and 4) are the same within the error of interpretation of the radiance patterns. (The ~20% unrecondensed water gas--whose (Rayleigh) scattering of sunlight is below the threshold of the video cameras--would be expanding much more rapidly outward; see Ref 4.)

In view of these observations we conclude that the small ice particles (or, at least, most of them) move with these much larger particles. (Atmospheric drag has no separating effect at Discovery's orbital altitude, as Appendix A states.) Thus the longitudinal velocity of the small particles in the ground images can be taken to be the velocity measured by following individual large, distinguishable drops in successive onboard images. In contrast to the aforementioned slow fractional decrease in size of the  $10^3$ -micron drops, the <1-micron ice drops sublime so rapidly that they become undetectable while they are still within the field of view of the groundbased camera, as we will find.

#### Stationarity of the Water Dump

The discharge of supply water from Shuttle Orbiter may be considered a time-stationary physical event over the data period, in view of its following venting and external geophysical conditions.

1) The flow rate is constant (at 19.4 g/s; no variability is resolvable from NASA's tables of the volume of water remaining in the storage tank during the dumping period).

2) The angle between the axis of the venting nozzle and the velocity vector of Discovery remains fixed (at 180°, with an uncertainty that we estimate from the precision of the vehicle-aspect and venting-system data to be less than 3°).

3) The geophysical factors that determine the heat balance of the ice particles have negligible variation over the relatively narrow range of latitudes and longitudes of the (constant altitude) trajectory. a) The change in solar irradiance due to out-scattering of direct sunlight by the lower atmosphere and in-scattering by the upper atmosphere is very

small (the full disk of the sun at tangent altitudes above at least 40 km illuminated the water trail in the images reproduced in Figure 2). b) Changes in the thermal earthshine that might result from solar heating near dawn are less than the uncertainty in the flux of this infrared radiation. c) Any change in the ambient air density would be very small (the heating effect of collisions is in any case negligible).

Thus the montage in Figure 2 represents a series of projections to the ground station of the same physical phenomenon, in which the viewing conditions--or "scene lighting"--change as follows over the -5-min data period.

4) The scattering of solar photons toward the camera from individual particles varies with the angle  $\eta_1$  between the sun and line of sight (in Figure 3). This dependence differs between the two particle sizes (see later Figure 9), and thus figures in the interpretation of the groundbased image data.

5) The sight path through the quasi-conical, optically-thin cloud, and therefore the apparent surface radiances of this volume, varies as  $(\sin [\text{angle } \eta_2 \text{ to the symmetry axis of the cloud}])^{-1}$  when  $\eta_2 > -10^\circ$ . (Angles  $\eta_2$  and  $\eta_3$  are also defined and plotted in Figure 3.)

6) The plate scale at Orbiter over the trajectory is proportional to  $(\text{range from AMOS})^{-1}$ .

7) The radiance and extinction of the sky vary with zenith angle  $\eta_3$ , although not so much as to affect the outcome of our data analysis even without being corrected for. a) Nightglow intensities from the upper atmosphere vary with  $(\cos \eta_3)^{-1}$  when  $\eta_3 < -75^\circ$ ; however the baseline in the groundbased images is not due to this scene background, but arises principally from dark current (see later Figure 11, for example). b) Zodiacal light radiances increase as the sight path from the ground station passes closer to the sun, both in and out of the ecliptic plane; this smaller component of the natural brightness of the night sky is also below the camera threshold. c) Attenuation of the optical signal due to out-scattering above AMOS also increases

with  $\eta_3$ ; however since the transmission (averaged over the camera's sensitivity and sunlight spectrum) of the near-Rayleigh atmospheres typical of this mountaintop station is as high as 0.85 in the zenith and decreases only to 0.7 at  $\eta_3 = 60^\circ$  (as shown by LOWTRAN calculations), when the other uncertainties in absolute radiometry are considered the small extinction of the solar radiation scattered toward the camera by the particles can also be neglected.

In view of this physical stationarity of the water venting, a photometric-photogrammetric analysis of a single video frame would provide sufficient information about the mean radii and concentrations of the sunlight-scattering particles responsible for the signal at the ground camera. The aforementioned dependence of the brightnesses along the trail on  $\eta_1$  further serves to distinguish between the two particle sizes.

## 5. Telescope-Camera

### 5.1 Specifications

The groundbased sensor is an intensified video finder camera precisely mechanically coaligned with (by being fixed to) the 1.2-m diameter "MOTIF" space object-tracking telescope. We review for background purposes its operating parameters, which we took from drawings in the AMOS Users' Manual (Ref 10), information provided informally by AMOS staff, and specifications of generic ISIT image tubes.

The camera's  $0.40^\circ \times 0.30^\circ$  angular field is set by the physical area of its first-stage intensifier's focal plane. The S-20R response of this photodetector can be adequately well approximated for our purposes by upper and lower half-peak photon sensitivities at 0.4 and  $0.65 \mu\text{m}$  (taking into consideration the decrease toward the red of the spectrum of sunlight and the increase toward the blue of the small atmospheric attenuation above AMOS, and assuming essentially-uniform transmission of the largely-reflective finder telescope itself). Fiber optic couplers then transfer the amplified image to a silicon

intensified-target video receiver tube. The electronic gain of the camera was manually changed several times over the exposure sequence in Figure 2, presumably by applying the condition that the video amplifiers not be severely overdriven by sunlight scattered from Discovery's body while the image of the water trail remained above noise on the camera operator's display monitor (and the videotape record).

Tracking on Discovery's body from its orbital elements appears stable to less than at most 3 picture elements (total width), or 1/200 of the full video image field. Thus tracking jitter introduces negligible photogrammetric error when successive frames [in which the aspect angle of the water-particle trail is changing slowly] are directly coadded to improve the photometric signal/noise ratios. We averaged neighboring frames by first transcribing the analog video record to VHS format, and then digitizing these data to a 512 x 512 pixel, 8-bit gray scale stored as a binary disk file.

## 5.2 Photometry

From the 55-cm clear aperture of the objective lens and the field demagnification, and diagrams of the camera's optics in the Users' Manual, we calculate its effective aperture ratio to be f/4. At 60° zenith angle the total brightness of the moonless night sky between 0.4 and 0.65  $\mu\text{m}$  (which as alluded to above is due mainly to airglow) is about 6000 Rayleighs, which is  $10^{-10} \text{ w/cm}^2\text{-sr}$ . In an f/4 optical system without transmission losses this scene radiance would result in an irradiance of about  $10^{-11} \text{ w/cm}^2$  at the photocathode. With 100 lumens/watt adopted for the nightglow spectrum (to convert to the illumination-engineering units in which commercial video systems are specified), this irradiance becomes  $10^{-6}$  foot-candles. Manufacturers' specifications for ISIT cameras--the RCA 4849/H series, for example--state that this cathode illumination would produce photocurrents somewhat smaller than the dark current (when the tube is operated at temperatures near 20°C, with the



recommended high voltage applied). The phototube in the AMOS camera is known to have been in service for several years, and the actual dark current under its present operating conditions is not known.

If the "background" photocurrents in the groundbased video images (which reproduce as dark areas in Figure 2) were principally signal from the night sky, this known radiance would provide a reference for determining the absolute radiances of the overlying water-particle trail. (Near the edges of the video frame this pixel current is 61 of 256 digitization units in Figures 4-6.) Should identification of the generally-faint stars that streak through the very narrow field of view prove possible, although a usefully-accurate "calibration scale" of visible radiances could not in practice be derived from their magnitudes (i.e., irradiances) they would serve for verifying the absolute trail radiances that we estimate later. (The strongly-bloomed images of Shuttle Orbiter are not useful for photometry.) We return to the question of output currents from background-sky illumination relative to instrument dark current in our interpretation in Section 9 of the brightnesses of the sunlit trail.

Quantification of the scene radiances from the video signals requires a known relation between this output current--the experiment observable--and the input irradiance at the camera's image plane--to which the physical quantity of interest, the radiance, is proportional. The performance specifications for ISITs show that near threshold their incremental currents are directly proportional to the incremental irradiances, and that the slope of this response characteristic decreases as saturation output current is approached (as would be expected; ISITs count photons somewhat like electron multiplier-based phototubes). We interpret the effect of varying the electronic amplification of the telescope-camera as merely changing the systems's initial response proportionality factor or "contrast", and concurrently its dynamic range (in practice, the noise-equivalent irradiance

most probably also depends on video gain). We therefore adopt a linear relationship between the photocurrents and the visible radiances of the water trail (after the "background" from system dark noise plus real night-sky emission is subtracted out), with the recognition that some error will be present near saturation --principally, in that segment of the trail within a few hundred m from Shuttle Orbiter.

### 5.3 Overview of the Ground Images

The very high irradiances at AMOS due to scattering of sunlight from Orbiter's high-albedo body result in the blooming of and undershoot in its image evident in Figure 2. This irradiance signal is expressed by NASA as equivalent stellar visual magnitude after a (nominal) correction for extinction by the intervening atmosphere; if Discovery were to scatter isotropically, its magnitude would vary with  $(\text{range})^{-2}$  where this attenuation is small. Some typical such NASA-defined equivalent magnitudes are given in the caption of Figure 2.

While the aforementioned changes in its gain are evident in the videotape, no record was kept of the relative photocurrent-to-irradiance response of the camera system. Hence the apparent brightnesses in the reproductions in Figure 2, which we made by photographing single captured frames displayed on a video monitor screen at a fixed exposure time, would not accurately represent the actual trail brightnesses. Further, the variability in apparent length of the glow volume (above that due to the changing plate scale and aspect) is also an effect of camera threshold (the angular spread of this glow, which would have less dependence on system sensitivity, remains more or less the same within the rather large measurement uncertainty).

The image of the trail at 15:23:40-41 (Figure 2c) shows particularly good contrast due to its combination of small--i.e., "forward"--solar scattering angle  $\eta_1$  ( $48^\circ$ ), small aspect angle  $\eta_2$  ( $33^\circ$ , so that the sight path length is about twice that in perpendicular projections), and relatively long range to Orbiter

(NASA stellar magnitude +34; the low irradiances from the vehicle body presumably allowed the camera operator to increase the electronic gain and thus enhance the extended radiating volume). Contrast and area-above-baseline of the water trail against background is lower when Discovery is near the zenith; as alluded to in the previous paragraph, the glow appears to occupy a smaller area in these images because of its lower projected radiances and the generally-higher threshold of the sensor. This finding is somewhat unfortunate, as the geometry of the particle cloud would be less subject to error from rectification in projections more nearly perpendicular to its long axis.

We selected this image with Discovery at 61° zenith, 70° azimuth for digital processing and analysis. Figure 4 is a contour plot of the photocurrents from individual pixels, averaged over 15 successive 1/30-sec video frames; we take these currents-over-baseline to be proportional to the radiances from the trail, as discussed in the immediately-previous subsection. Figures 5a and 6 are longitudinal (long-axis, corrected for  $\eta_2$ ) and transverse one-dimensional radiance traces from this averaged scene. We stress again that the spatial and size distributions of the two types of ice particle remain the same during the water-venting period (for the less-numerous explosion-product particles this statement holds in a statistical sense); this particular two-dimensional projection of the three-dimensional volume scattering rate pattern is judged to have the best signal/noise ratios for characterizing these distributions.

## 6. Onboard Cameras

### 6.1 General

The onboard cameras, although also radiometrically uncalibrated, provide useful data on the number, longitudinal velocity (determined in the next subsection), and--qualitatively--irradiances of the millimeter particles relative to those from the accompanying cloud of unresolved submicron particles. We apply this information later in calculating a mean "diameter" of

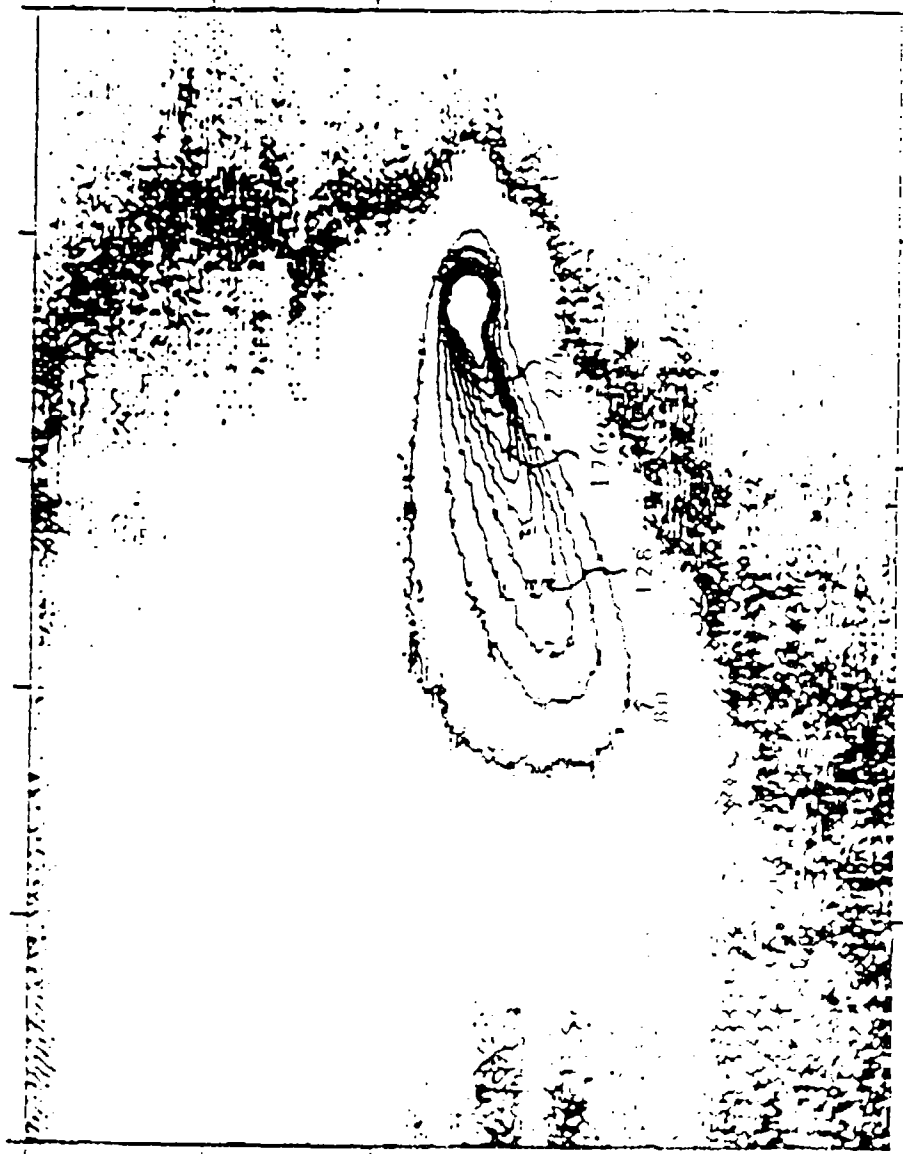


Figure 4. Equi-photocurrent contour plot of the groundbased image in Figure 2c. The contours are separated by 16 of 256 digitization units. The pattern of scattered sunlight from the water particles appears to extend almost to the frame edges. The initial ~600 m of the trail is severely contaminated by blooming from Orbiter's body (NASA equivalent stellar magnitude 3.6). The glow ahead of the spacecraft is an instrumental effect. See also Figures 5 and 6.

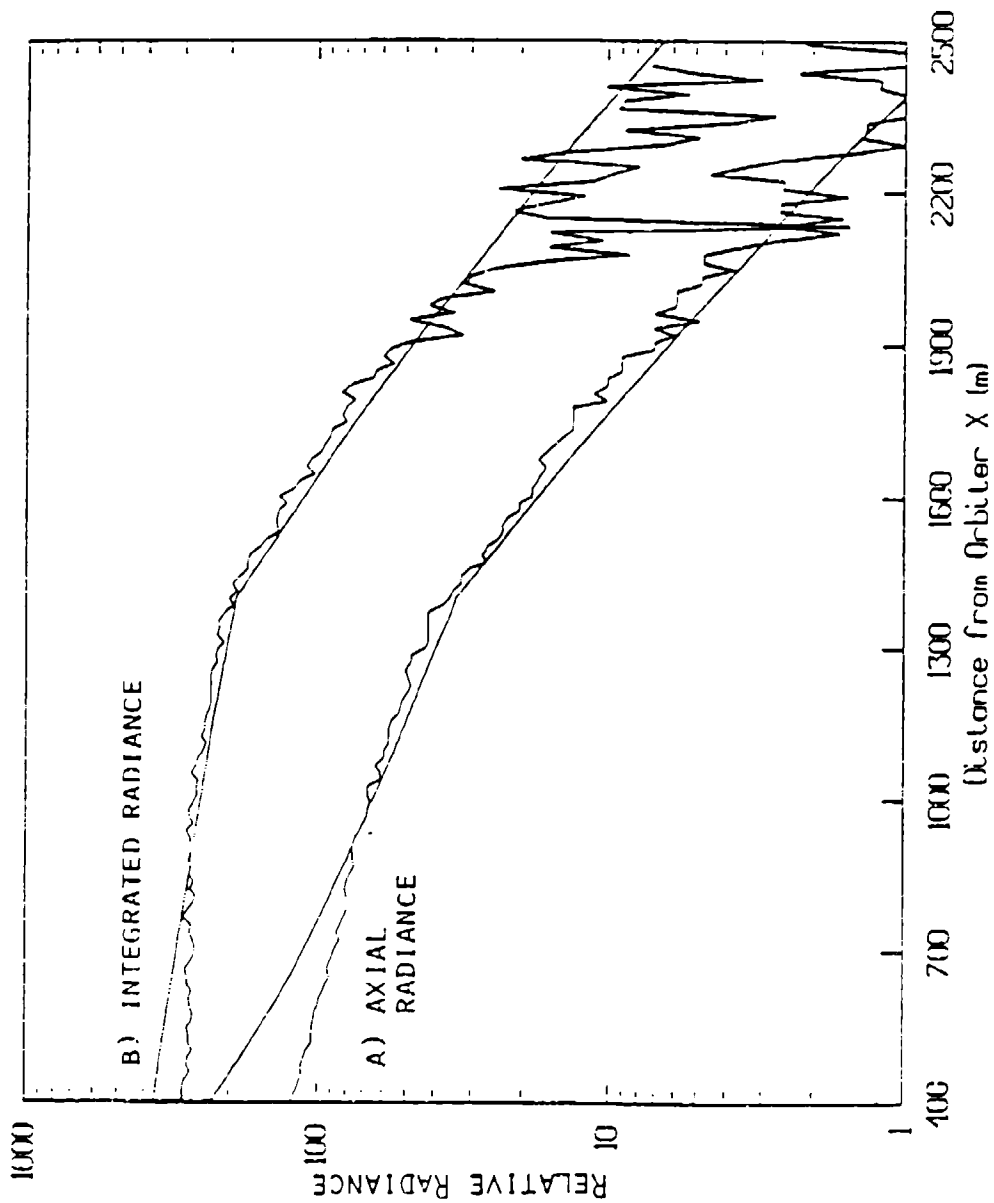
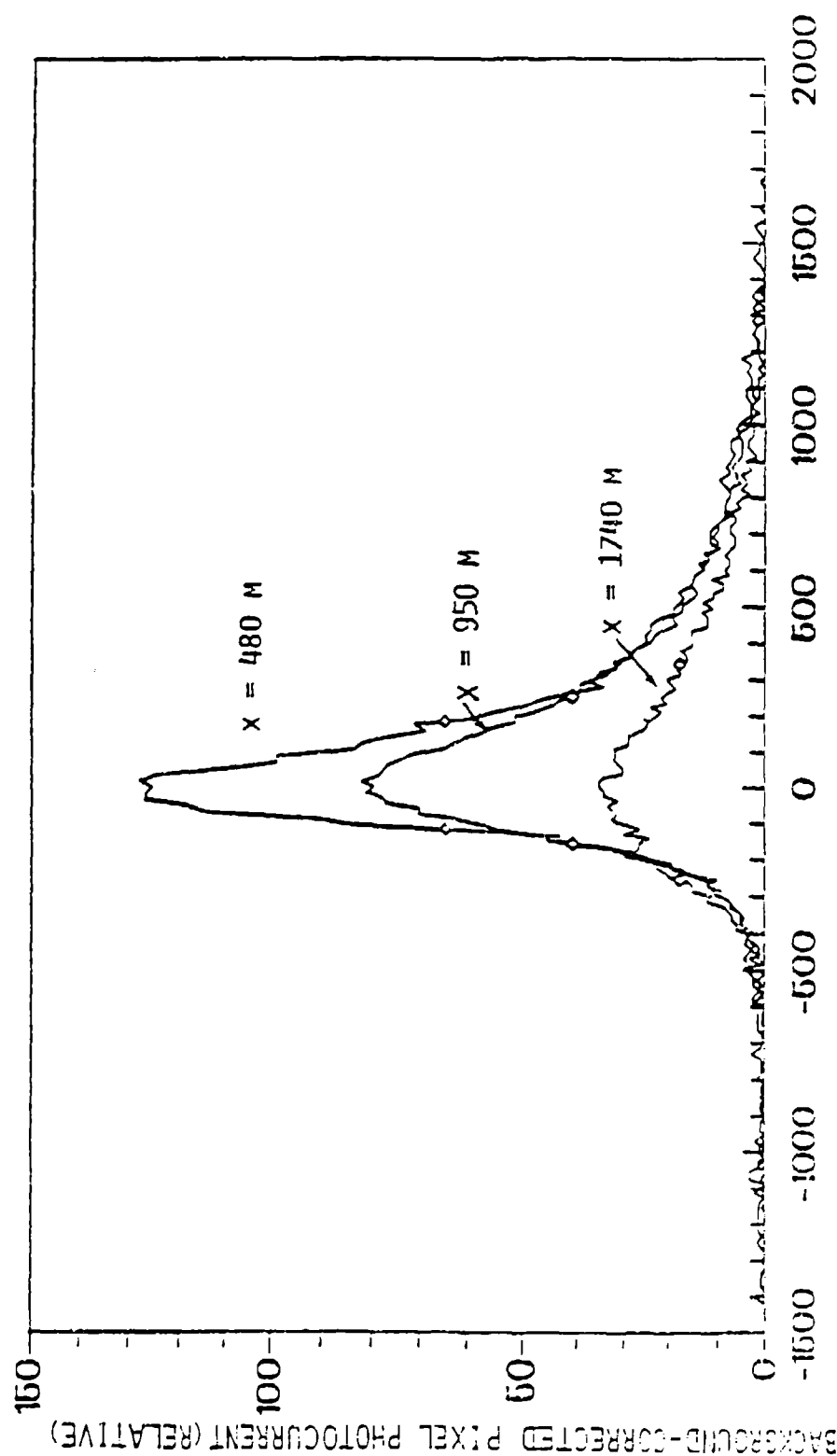


Figure 5. a) Relative radiance along the line of maximum brightness extending out from Discovery in Figure 4, with background subtracted (and a linear relationship between the video photocurrent and scene radiance assumed). b) Radiances summed along lines transverse to this long axis (integrated radiance). The smooth curves represent a two-parameter fit to the sublimation rate as shown in the text.



DISTANCE FROM APPARENT CENTERLINE OF WATER TRAIL (M)

Figure 6. Relative radiances along lines transverse to the long axis of the trail in Figure 4 at the downstream distances  $X$  indicated. The decrease in these integrated radiances indicates qualitatively that the radii of the ice particles are decreasing. Figure 5 a) shows the peaks of these curves, and Figure 5 b) plots the areas underneath them.

the large droplets and the fraction of vented water in the small droplets.

Typical projections of the trail to the handheld video camera pointed out of the crew-cabin window by a mission specialist and the more distant operations-documenting camera in Orbiter's bay are in Figures 1a and b and Figures 7 and 8. Comparison with Figure 1c, reproduced from Figure 8 of the report of Ref 7's injection of water with temperature 20°C, velocity 9 m/s, and nozzle diameter 3 mm, indicates that the phenomenology of Discovery's venting is at least qualitatively similar to that observed in this laboratory experiment.

## 6.2 Photometry and Photogrammetry

Space shuttle's closed-circuit documentary cameras (Ref 11) use silicon intensified-target video receiver tubes (of the RCA 4804H family), which have substantially higher irradiance thresholds than ISITs. An object position-sensing automatic electronic gain and iris control provides wide inter-scene dynamic range while protecting against overcompensation when very bright objects--such as Orbiter's sunlit bay--lie near the edge of the field of view. Focus, pan and tilt angles, and angular field are controlled from the crew cabin with the aid of a monochrome video monitor. (Some of these cameras have three-color separation capability, through a rotating filter wheel in the optical system.) The dependence of output current on irradiance can be varied manually, with one dial setting providing a linear response. The cameras operate at standard broadcast video (EIA RS-170) frame rates.

The west-southwestward-flowing (relative to Discovery) particle stream lies in the hemisphere away from the sun, which is southeast of the spacecraft during the data period. Thus the Mie scattering intensities vary along the retrograde trail with angle to the bay camera (in Figures 1a and 7), as indicated in Figure 9 and discussed below. Although these onboard cameras do not identify frame times (or el-az or zoom or gain settings),

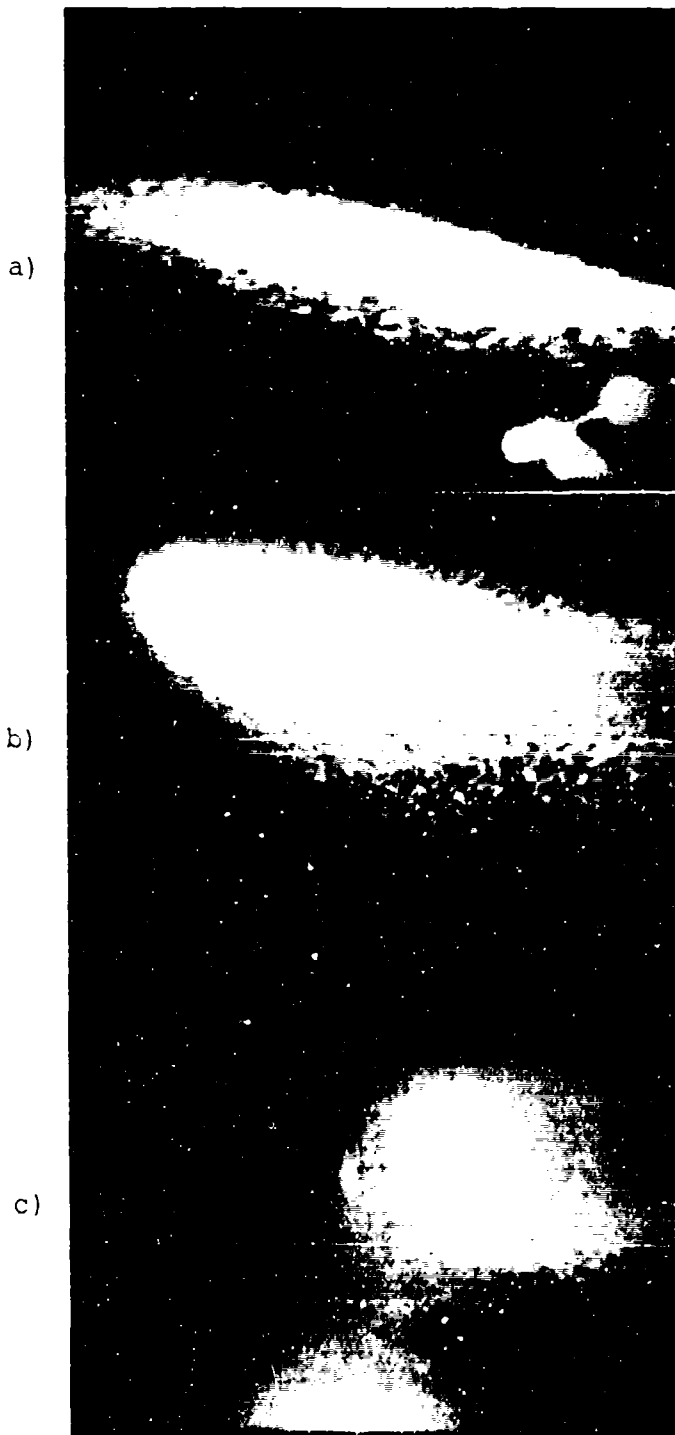


Figure 7. Views of the backlit water trail from the aft camera at three plate scales and increasing pointing azimuths. a), taken with a  $48^\circ$  horizontal field, shows what we interpret as the rainbow-angle region near the bright center of the frame; see also Figure 1 b). The determination of particle velocity was made from successive frames at this zoom setting and exposure. b) shows the vanishing point of the trail, at upper left. Some of the individual large droplets scatter sufficiently strongly to produce dark undershoots in the video electronics; other dark areas in the images are most likely areas of low particle density.



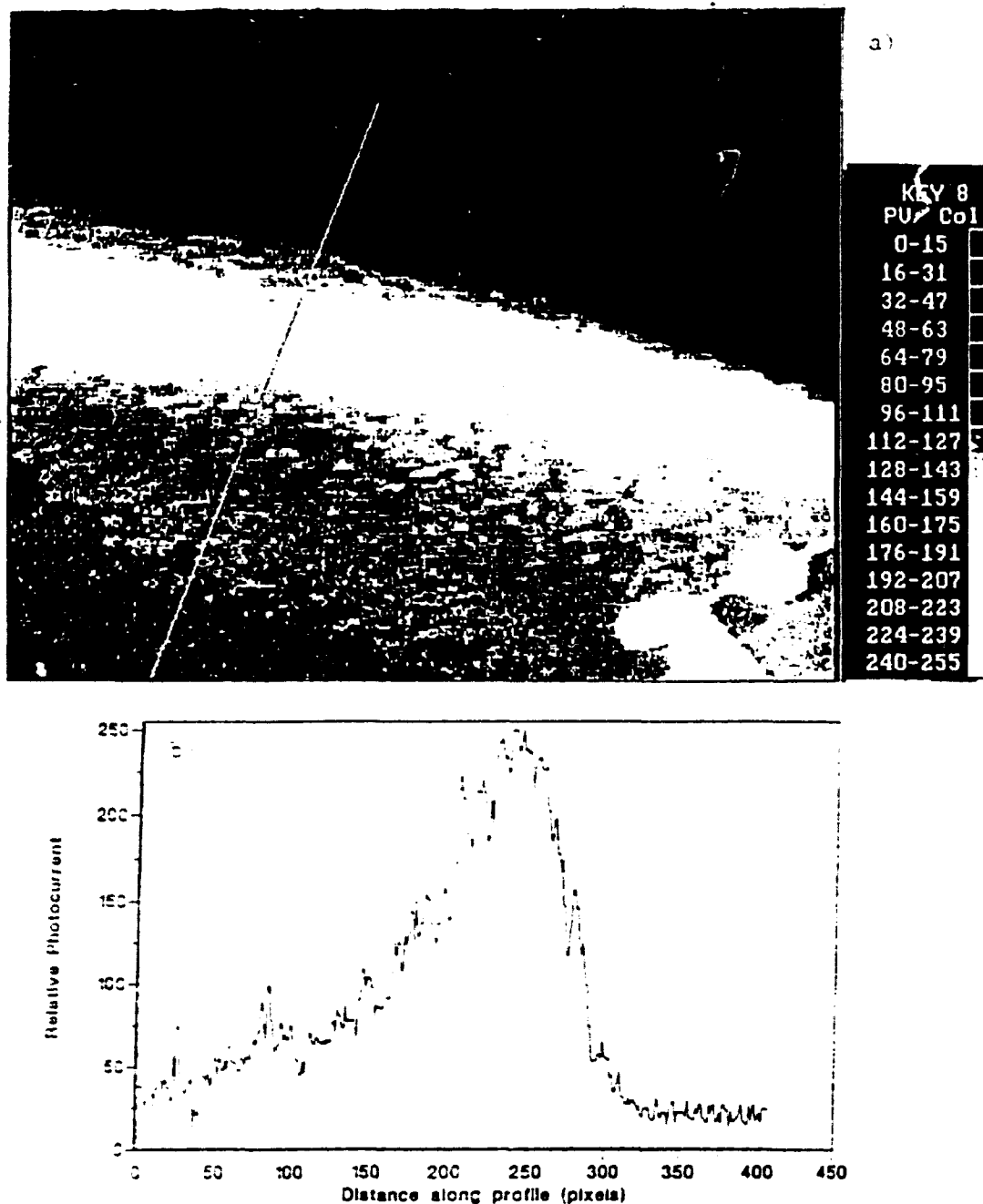


Figure 8. View of the water trail from the payload bay aft video camera (Figure 7a); estimated horizontal angular field is  $48^\circ$ . a) Digitized image frame. Payload bay structure is visible at lower right. b) Profile across image along diagonal line in a). The origin of the profile corresponds to the lower left endpoint of ling segment, and the plane of the profile intersects the trail axis at  $-26$  m from the nozzle, where the solar scatter angle is  $-140^\circ$ .

Discovery's latitude/longitude and therefore these sunlight-scatter angles could be estimated from positions along the videotape between the start of sunlight illumination of the water trail and of meteorological clouds near local dawn. We judged this effort unnecessary, since no absolute calibration exists of the image plane irradiances (which would be needed for using them to determine the particle sizes).

### 6.3 Overview of the Onboard Images

The principal qualitative impression from playbacks of the onboard-video records is of a spatially dense (but optically thin) stream of discrete particles with a relatively broad size distribution--as evidenced from the variability of the irradiances from particles at fixed downstream distances--, moving away from the spacecraft at constant speeds that vary by <10% among individual identifiable sunlight-scattering centers. (That the cloud is optically thin is verified by the gradients and calculated absolute magnitudes of the radiances in the projection to the groundbased camera, and from the concentrations of the large particles.)

While physical structure on these expected mm-diameter droplets is of course far below the 10's-cm lateral spatial resolution limit of either onboard video camera at the range of the trail, some particles appear to flicker (with periods roughly  $\frac{1}{4}$  second). This modulation of their sterance shows that these are tumbling irregular ice/snow as seen in the laboratory simulation of Ref 6, rather than spherical liquid (or even ice) drops. Further evidence that the phenomenology of the vented water stream is similar to that in the space-tank experiments comes from the spatial density of these macroscopic particles, which we count from the video images to be  $100 \pm 50$  (10 estimated error) per meter of longitudinal path--a number consistent with the mass flow rate and expected mean size of the droplets.

#### 6.3.1 Cabin Camera

This handheld camera views an about 20- to 100-m long segment of the flow path (depending on where it is pointed), which starts as close as 5 m from the venting orifice. The angular divergence of the radiation pattern indicates that the liquid stream explodes within a very few m from the nozzle, indeed perhaps within a few cm. Background to this camera is the celestial scene near the horizon; no stars appear, presumably because the strong signal from reflected cabin lights and the close-lying sunlit particles themselves force down the automatically-controlled video gain. As we mentioned above, the irregular structure evident in the example of Figure 1a is qualitatively similar to that in the view (from much closer) of laboratory water stream in Figure 1c. The angular spread of the macroscopic-droplet stream in the projection to this camera is about the same as that inferred from the groundbased images.

#### 6.3.2 Tail Camera

This camera, located at the rear of Shuttle's bay (at station 1290, -87, 446), was operated remotely by Discovery's flight crew, who varied its angular field as well as its azimuth during the data period. Its background is the ocean surface (and some cirrus clouds, which appear in the late-time, after-dawn images) illuminated by nightglow and astronomical sources. Arrays of discrete lights, in all probability those of the Hawaiian Islands, occasionally pass across the scenes.

When part of Discovery's sunlit bay is in this camera's field (as in Figure 1b and 7a), the decreased video gain reduces the photocurrents from the trail; in these projections, some 200 m longitudinally starting about 5 m from the venting nozzle fit into the image. (A field of view angle is estimated in the next subsection.) The low surface brightness of the cloud within the first few m from the nozzle (see in particular Figure 1b) is most probably due to shadowing by Discovery's body, as the sun is on the opposite side of the spacecraft. The observed divergence of

the particle cloud again indicates that its apex is within a very few m of the nozzle, and the angular spread in these projections is also the same within experimental error as that seen from the ground station.

We interpret the bright region to the right of center in Figure 7a as a rainbow, that is, the order-of-magnitude increase near  $137^\circ$  scattering angle in the differential cross-sections of large spherical ice droplets; refer to Figure 9. Figure 8 is an equi-photocurrent contour plot from this frame (with the high spatial frequencies from the individual particles filtered out), and a transverse trace at -26 m downstream from the nozzle. The brightness asymmetry, with the steeper edge toward the earth, is seen also in the groundbased images (Figure 2); it may be due to imperfections in the water-venting nozzle. The absolute image irradiances produced by the -mm-diameter particles can be estimated from their differential scattering cross-sections and mean ranges to the camera, as is done below.

In Figure 7b the aspect angles of the cloud are generally smaller, so that the sight pathlengths are longer and thus the radiances are higher. (No geometric reference is available to fix the angular field and pointing of the camera axis.) In Figure 7c the camera points at a larger azimuth angle from Orbiter, at a still shallower mean aspect that further increases the projected trail brightnesses. The bright area near the center of the field in Figure 7c is most likely an artefact of system response to the bright scene. The vanishing point of the trail is within the field of view in these two latter frames.

The bloomed images of these densely-packed, discrete large particles produce a spatially continuous overlay of apparent brightness (in each projection to onboard) that is indistinguishable from any radiance which would be produced by scattering of sunlight from the accompanying cloud of unresolved small particles. As Figures 1 and 7 show (and as we stated earlier), this "haze" does not extend beyond the distinguishable particles.

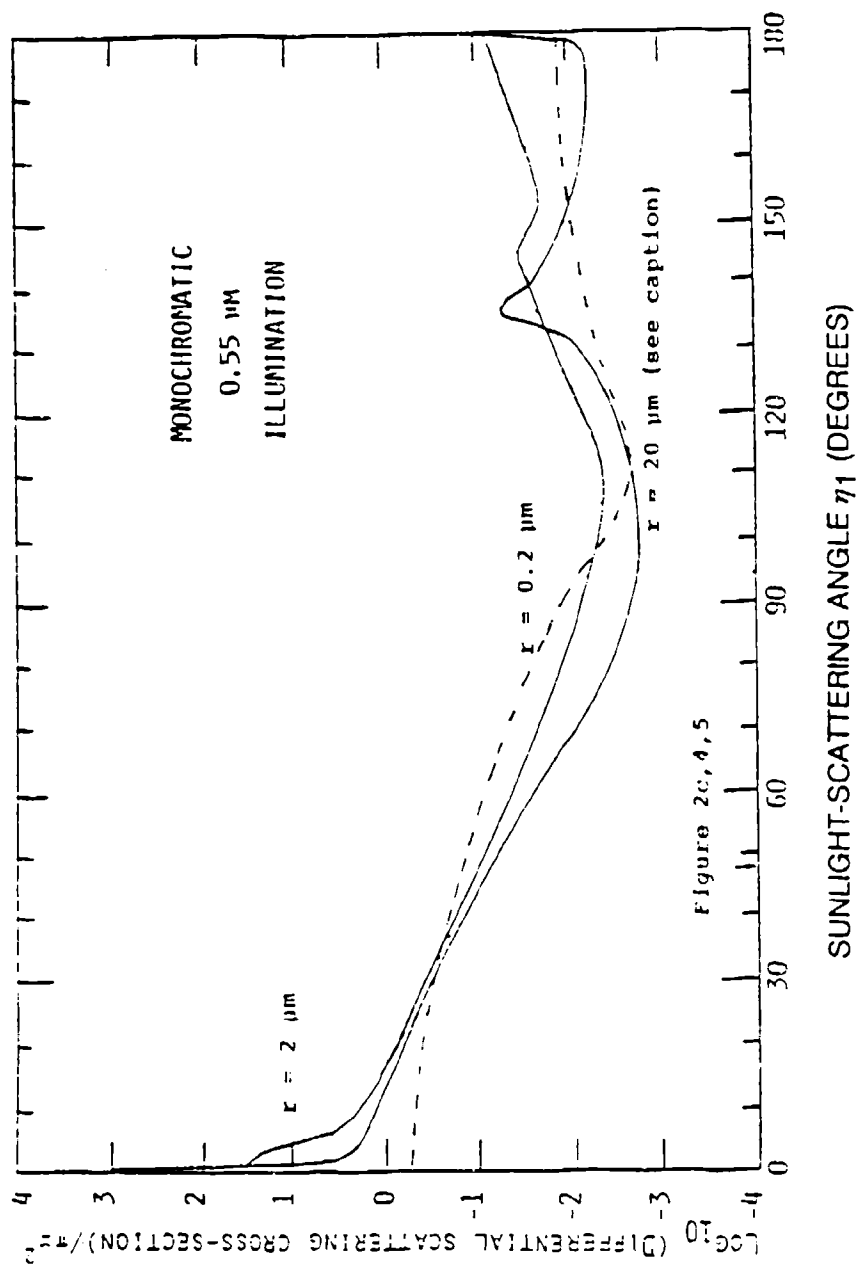


Figure 9. Photometric scattering functions of 0.2  $\mu\text{m}$ , 2  $\mu\text{m}$ , and 20  $\mu\text{m}$  radius ice particles under 0.55  $\mu\text{m}$  illumination (average of both polarizations). We manually suppressed the Mie oscillations for the two larger-radius particles in transcribing the scattering function, as they are damped by the 0.25  $\mu\text{m}$  range of wavelengths of illumination and detection in the AMOS images. The curve labeled  $r = 20 \mu\text{m}$  is valid to within a factor  $1\frac{1}{2}$  for radius  $r > 10 \mu\text{m}$ . Pure Rayleigh scattering (radius  $< 0.05 \mu\text{m}$ ,  $1 + \cos^2 \eta_1$  dependence) would exhibit only the usual factor 2 variation between  $0^\circ$  and  $90^\circ$ .

in the transverse direction; thus if this continuous radiation is indeed in substantial part due to the small particles their radial velocities are about the same as those of the large (direct explosion-product) particles.

### 6.3.3 Outboard Camera

A video camera on Discovery's Remote Manipulator Arm documented a different (but presumably; physically similar) supply-water dump from that illustrated in Figures 1, 2, and 7. As this camera was viewing the trail against Orbiter's also-sunlit protective tiles, its images exhibit lower contrast. The liquid stream appears to remain coherent out to roughly  $\frac{1}{2}$  m from the nozzle (that is, for about 20 milliseconds, as we show in the next Section), and then breaks up into a cone of radially-irregular surface radiance within a distance that varies by less than 10% (the practical spatial resolution limit) during the -5-min data period. The mean angular spread of the streaking particles is again the same within experimental error as in the other onboard images, with a similar frame-to-frame lateral variability (due to the statistical distribution of sizes and transverse velocities the cavitation-breakup products).

The videotape from this Remote Manipulator Arm camera also includes a venting of waste water (respiration products and urine; particulars are in Ref 2), at an unspecified rate and temperature. This stream explodes within a very few cm of the nozzle, into a noticeably smaller half-angle quasicone than the supply water. Such an earlier onset of flow instability would be expected from the at least an order of magnitude higher concentration of gases and the bubble-seeding impurities in the liquid (Ref 4). The smaller transverse velocity can also be inferred from the photographs of the laboratory simulations (although this point is not explicitly discussed in the literature); apparently the larger number of bubbles in the impure superheated water impart less energy to the liquid as they

cause its surface tension forces to fragment it into discrete droplets.

#### 7. Velocity of the Large Ice Particles

We measured the longitudinal velocities of identifiable large ice particles from their positions in successive video frames from the aft onboard zoom camera (as in Figure 7a). The images from the crew-cabin camera are less suitable for this purpose, as they lack visual references for estimating the angular field and--in particular--the mean range to the segment of trail within this field.

The camera just forward of Orbiter's vertical stabilizer views the trail to within  $14^\circ$  from perpendicular to the trail axis, where the sunlit particles emerge from behind Discovery's open bay door (into what appears to be principally scattered sunlight). We determined the camera's horizontal field of view at the time of the velocity measurements from the angle subtended by a radiator panel mounted along this door, which we identified on scale drawings of Shuttle Orbiter. This object measures 1.5 m transverse to its direction to the bay camera, is on average 9.6 m distant, and its image extends across 0.19 of this image frame. These dimensions would result from a full horizontal angular field of  $47\frac{1}{2}^\circ$ , with an uncertainty that we estimate as  $\pm 7^\circ$ . (Although the stated (in Ref 11) maximum field of view with the initially-specified zoom lenses is  $39.4^\circ$ , we have sufficient confidence in this measurement to use it henceforth; an  $80^\circ$ -horizontally alternative zoom lens has become qualified and available since the space shuttle camera system was first documented, and in any case adoption of the larger field results in an error of only 20% in the particle velocity and thus does not alter our conclusions about the phenomenology of water ventings.)

We advanced the videotape successively one full 1/30-second frame, recording the number of frames during which individual particles moved from  $27^\circ$  from the nozzle to  $39^\circ$ , which represents

a pathlength of 7.7 m. (An earlier effort to time the movement across the full horizontal camera field produced less reliable results, since the longitudinal distance traveled can not be accurately determined.) In 7 trials on high-irradiance droplets moving within 5° of the trail axis the number of video frames per such transit was 10, with a standard deviation of less than 1 (fractional frames could be estimated). This small spread indicates that these large particles have a narrow longitudinal velocity distribution, as would result if the velocities imparted to them when the expanding steam bubbles lead to breakup of the liquid stream were both small and principally radially-directed.

The mean speed along the trail axis measured by this procedure was 23 m/s. Taking into account the systematic errors in timing the transits and in the full and partial fields of view of the bay camera at the particle trajectories, we estimate the uncertainty of this measurement to be +25%, -35% (the latter being larger because of the above-mentioned potential inconsistency in our measurement of the zoom camera's horizontal field). This figure is consistent with an earlier, undocumented estimate of the longitudinal speed (in Ref 5), 9-23 m/s.

This velocity in free space can be compared with the velocity derived assuming fully developed Poiseuille flow in the conical nozzle (Ref 4), which is  $1.32 \cdot (\text{water volume vented per unit time}) / (\text{exit crosssectional area}) = 16 \text{ m/s}$ . The condition for achieving this free-stream velocity is that the Reynolds number in the nozzle (essentially,  $[\text{flow velocity}] \cdot [\text{diameter}] / [\text{viscosity}]$ ) be greater than about 100. The parameters for Discovery's venting place the Reynolds number much higher: the product of mass flow velocity and orifice diameter is about  $100 \text{ g cm}^{-1} \text{ s}^{-1}$ , while the viscosity of water at 60°C is near  $0.005 \text{ g cm}^{-1} \text{ s}^{-1}$ . The ejected stream contracts to  $0.87 \times 1.4 \text{ mm} = 1.2 \text{ mm}$  as its radial velocity profile relaxes to uniform from parabolic (i.e., Poiseuille) at the nozzle exit, with the average speed increasing by 32%.



As discussed earlier, the cavitation breakup of the coherent stream several cm from the vehicle body would not impart a net longitudinal velocity to the product droplets. We conclude, then, that the mean particle velocity that we measured 10's m into the wake trail is consistent with steady Poiseuille flow in the nozzle followed by relaxation to a radially-uniform flow velocity distribution in the liquid stream before it ruptures.

#### 8. Photometric Analysis of the AMOS Video Images

We show next that the visible radiances in the projection to the ground station are due principally to the submicron-diameter recondensation ice particles, and that the observed rate of decrease of mean sunlight scattering cross-section of these small droplets is consistent with standard radiation theory when a modest correction is applied for the increasing sublimation rates as the surfaces of the particles roughen. We then estimate the sizes and abundances of both the millimeter and submicron particles from the relative image irradiances that each component produces at the distant and close-lying cameras. The detailed calculations of the radius and temperature history of the small particles are presented as Appendixes A and B, and the temperature and infrared radiances of the cloud of large particles are derived in Appendixes C and D.

We focus the analysis of the AMOS camera data on the frame reproduced in Figure 2c and (in radiance contour form) Figure 4, from which follow the plots of background-subtracted axial brightness in Figure 5a and transverse-summed brightnesses per unit trail length of Figure 5b. This latter quantity--sterance per unit flow path, sometimes referred to as station radiance--is also the area underneath the curves of brightness perpendicular to the trail axis in Figure 6.

The critical qualitative feature of Figure 5b (and Figure 6) is the decrease in this spatially-integrated surface radiance with distance from Discovery's venting nozzle, which immediately

shows that the individual sunlight-scatterer particles responsible for the signal at AMOS lose a substantial fraction of their optical cross-section--which is to say, volume--within the instrumentally-detectable  $\sim 2\frac{1}{2}$  km length of the trail. Appendix C shows that mm-diameter ice droplets would lose less than 2% of their radius in the transit time beyond the bloomed pixels ( $\sim 2000$  m /  $20 \text{ m s}^{-1} \approx 100 \text{ s}$ ), and therefore could not account for the two orders of magnitude decreases in radiance observed. In contrast, such a large change would result from the sublimation of the much smaller recondensation ice particles (Appendix A).

The conclusion that the surface brightnesses in the projection to AMOS result primarily from scattering of sunlight by these submicron particles is semiquantitatively supported by the dependence of the mean visible radiances of the trail on the solar-scattering angle  $\eta_1$ . This angle decreases from  $90^\circ$  (16 s after Figure 2b, before which excessive blooming from the spacecraft's body precludes even a qualitative estimation of the trail brightnesses), to about  $30^\circ$  toward the end of the data period. Despite the fact that the several electronic gain changes made over this range of  $\eta_1$  have an unquantified effect on both the signal and the camera's noise threshold, the increase in radiance at corresponding points along the trail (adjusted for the sight path effect of  $\eta_2$ ) can be estimated as less than about one order of magnitude (refer to the set of scenes in Figure 2). This change is consistent with Rayleigh or "near-Rayleigh" scattering (where  $2\pi[\text{particle radius } r]/[\text{photon wavelength } \lambda] < -1$ ), while in contrast strongly "geometric" scattering (where  $2\pi r/\lambda \gg 1$ ) would result in an increase of almost two orders of magnitude over this range of  $\eta_1$ , as is shown by the differential cross-sections in Figure 9.

A second striking feature in Figure 5b (and 5a) is the change in average slope that takes place over a distance of about 200 m near 1400 m from the venting nozzle. An important further observation is that the logarithmic radiance plot also exhibits some downward curvature, which is greater in the more-downstream

trail segment. The discontinuity in mean slope in the longitudinal photocurrent plots of Figure 5 is after-the-fact discernible in the continuous-tone image of Figure 2c, as a brighter inner region extending out from the bloomed spacecraft body.

The most obvious physical explanation of this discontinuity is that the near-spherical ice particles are undergoing a transition from the "geometric" scattering regime, where their cross section varies about as (radius)<sup>2</sup>, to the Rayleigh regime, where cross sections change much more rapidly--specifically, with (radius)<sup>6</sup>. That this hypothesis quantitatively explains the radiance dependences in Figure 5 is shown in Appendixes A and B, the principal conclusions of which are as follows.

[Appendix B]. The low earth-orbiting, sunlit particles reach an quasi-equilibrium temperature of about 180K within less than 1 s of their formation (that is, at ~20 m from Orbiter), after which they continue to sublimate at the much lower rates calculated in Appendixes A and B.

[Appendix A, 1]. The particle radius during this latter period decreases exponentially with time. Applying the wavelength- and radius-dependent emissivities of ice computed from Mie theory in balancing the heat gain by absorption of earthshine and direct sunlight against the heat loss by thermal graybody radiation and sublimation, we find that the absolute decrease of radius of smooth-surfaced spheres comes within less than a factor 2 of fitting the relative AMOS radiance-distribution data.

[Appendix A, 2]. The finite (and increasing with distance X from the spacecraft) curvature of the axial and transverse-summed brightnesses indicates that the sublimation rates are changing somewhat more rapidly than a pure exponential would indicate. A gradual roughening of the surfaces of the ice

particles, which is known from laboratory experiments to take place (Ref 12), increases the sublimation rates sufficiently to fit Figure 5 quantitatively.

The smooth line in Figure 5b is the fit to the groundbased data of a simple model of roughening-enhanced sublimation, in which the relative sublimation rate increases linearly with time after the small ice particles form. A discontinuity in scattering cross-sections follows naturally from the essentially geometric-to-essentially Rayleigh transition (which happens to take place near 1.4 km); and the progressive downward curvature is the direct consequence of the increasing irregularity of the surfaces of the small droplets. (The principal effect of the roughening is interpreted (Ref 12) as an increase in the imaginary component of the index of refraction and therefore the optical absorption, rather than as a gross change in exposed surface area.) Similarly, the smooth line in Figure 5a closely reproduces the radiances along the long axis of the particle trail, which differ from the transverse-summed radiances of Figure 5b only by the factor X that takes into account the the natural divergence of the wake direction-flowing cloud.

The mean radius of these small particles follows from the change in average slope that results from their transitioning into the Rayleigh scattering regime. We disregard the Mie oscillations in the differential cross-section, as these are largely washed out by the polychromatic solar illumination (and perhaps also by a somewhat-polydisperse droplet size distribution). The mean circumference of these particles at that transition position must be near the weighted-mean sunlight wavelength  $\bar{\lambda}$  ( $\approx 0.5 \mu\text{m}$ ), i.e.,  $2\pi r/\bar{\lambda} \approx 1$ . Note that particles with about this radius result in the most "efficient" scattering from a fixed total volume of ice (or water).

From the sublimation rates obtained from the fit to Figure 5, we estimate the initial radius  $r_0$  of these recondensation particles to lie between 0.15 and 0.3  $\mu\text{m}$  (Appendix A, Equation (A11); we neglect also the few-percent decrease in radius while

the particles are very rapidly cooling by sublimation from their 250K formation temperature to their equilibrium 166K). The corresponding interpretation of measurements in a space-simulation tank (Ref 8), with a 1.6-mm diameter, 65- $\mu$ s pulsed water stream at 20°C and somewhat higher total flow rate--that is, somewhat different venting conditions--, was  $0.08 \pm 0.03 \mu\text{m}$ .

We have assumed throughout this photometric analysis that the measured output currents from each pixel of the AMOS video system are directly proportional to the image-plane irradiances. This assumption, as we noted earlier, would not be valid near saturation, where the output currents from the ISIT increase less than linearly. We ascribe the deviation of the particle energy-balance model at high scene radiances--at  $X \leq 600$  m from Orbiter in Figure 5--to this downward curvature of the photocathode response characteristic.

#### 9. Absolute Brightnesses of the Submicron-Particle Cloud

We calculate from these radii and estimated column densities of the small particles the expected absolute radiances of the (optically-thin) trail in the projection of Figure 2c, and show in passing that the baselines in the AMOS images are most likely instrumental rather than due to the night sky background. Since we have already derived the relative  $0.4 - 0.65 \mu\text{m}$  axial brightnesses, an absolute brightness is needed at only one point along the trail [where the response of the camera is linear]. As mentioned earlier, the fraction  $f_m$  of the total ejected water mass  $M'$  that recondenses to form the submicron ice particles depends on the venting conditions; we adopt the fraction derived later from the groundbased and onboard video camera images, 0.3%, for estimating this absolute brightness. (The radiances of the sunlit trail are directly proportional to  $f_m$ .)

The number density  $n_m(X)$  of submicron particles on the long axis of the assumed-conical trail at distance  $X$  from the spacecraft is to a close approximation

$$n_m(X) = f_m M' / (4[X \tan \theta]^2 \cdot v), \quad (1)$$

where the subscript  $m$  denotes these particles.  $\theta \approx 15^\circ$  is the half-angle of divergence of the flow observed in the AMOS image,  $v \approx 20$  m/s the axial velocity of the particles relative to Orbiter (in view of the other geometric approximations we have rounded off the velocity derived above to one significant figure), and

$$f_m M' = f_m (dM'/dt) / ([4\pi/3] r_o^3 \rho) \quad (2)$$

is the rate at which the small particles are produced by recondensation of vaporized water molecules. Here  $dM'/dt = 19.4$  g/s is the mass flow rate of the vented liquid stream,  $\rho = 0.92$  g/cm<sup>3</sup> is the density of ice at temperatures near 200K, and  $r_o = 0.3$   $\mu$ m is the best-estimate initial mean radius of these droplets (as derived in Appendix A and the preceding subsection).

The volume  $V$  of the elliptical slab of sunlight-scattering particles containing the line-of-sight from AMOS to the axial point at  $X$  is

$$V(X) \approx \pi \Delta (X \tan \theta)^2 (\sin \eta_2)^{-1}, \quad (3)$$

where  $\eta_2 = 33\frac{1}{2}^\circ$  is the view aspect angle (Figure 3) and  $\Delta$  (which is small compared with  $X$ ) is the thickness of the conic section. The irradiance  $I_m$  at AMOS from volume  $V$  is then

$$I_m \approx I_{\text{sun}} (dC_{\text{SC}}/d\Omega)_m n_m(X) V(X) R^{-2}, \quad (4)$$

where  $I_{\text{sun}} = 4 \times 10^{-2}$  w/cm<sup>2</sup> is the solar spectral irradiance between 0.4 and 0.65  $\mu$ m (taken from LOWTRAN),  $(dC_{\text{SC}}/d\Omega)_m$  is the differential scattering cross section of individual small particles at  $\eta_1 = 48^\circ$  for photons of mean wavelength  $\lambda = 0.5$   $\mu$ m, and  $R = 637$  km is the range of the particle cloud from AMOS in Figure 2c. (We neglect the aforementioned small extinction by

the atmosphere, and continue to approximate  $n(X)$  as constant out to half-angle  $\theta$  within  $V(X)$ .) The surface brightness  $B_m$  of the cloud is then

$$B_m = I_m R^2 / (\Delta X \tan \theta), \quad (5)$$

where  $\Delta X \tan \theta$  is the area of volume  $V(X)$  projected along the line of sight. Substitution of Equations (1) - (4) into Equation (5) yields

$$B_m \approx I_{\text{sun}} (dC_{\text{SC}}/d\Omega)_m f_m M' \pi (4v X \tan \theta \sin \eta_2)^{-1}. \quad (6)$$

At  $X = 1$  km the mean radius of the small ice particles has decreased to about  $0.18 \mu\text{m}$ . From standard Mie theory (see Figure 9),  $(dC_{\text{SC}}/d\Omega)_m = 1.2 \times 10^{-10} \text{ cm}^2 \text{sr}^{-1}$ . Substitution of the numerical values into Equation (6) gives

$$B_m \approx 2 \times 10^{-7} \text{ w/cm}^2 \text{sr} \quad \text{at } X = 1 \text{ km}$$

as the predicted absolute  $0.4 - 0.65 \mu\text{m}$  radiance of the submicron cloud in Figure 2c [viewed at  $33^\circ$  aspect angle along its symmetry axis]. Figure 10 re-plots the axial brightnesses of Figure 5a on this "absolute" scale, along with the brightnesses that would result from scattering of sunlight by approximated-as-spherical large particles with two physically-reasonable mean diameters and the brightness of the moonless night sky at  $60^\circ$  zenith angle that we estimated above. Since the photocurrents produced by the trail are only up to about three times larger than those of the scene background in Figure 2c, we conclude from a comparison to the calculated radiances in Figure 10 that this baseline must be almost completely due to the dark current of the AMOS video camera.

An expression analogous to Equation (6) applies to the surface radiances of the underlying cloud of large, polydisperse (and still approximated as spherical) ice particles in the

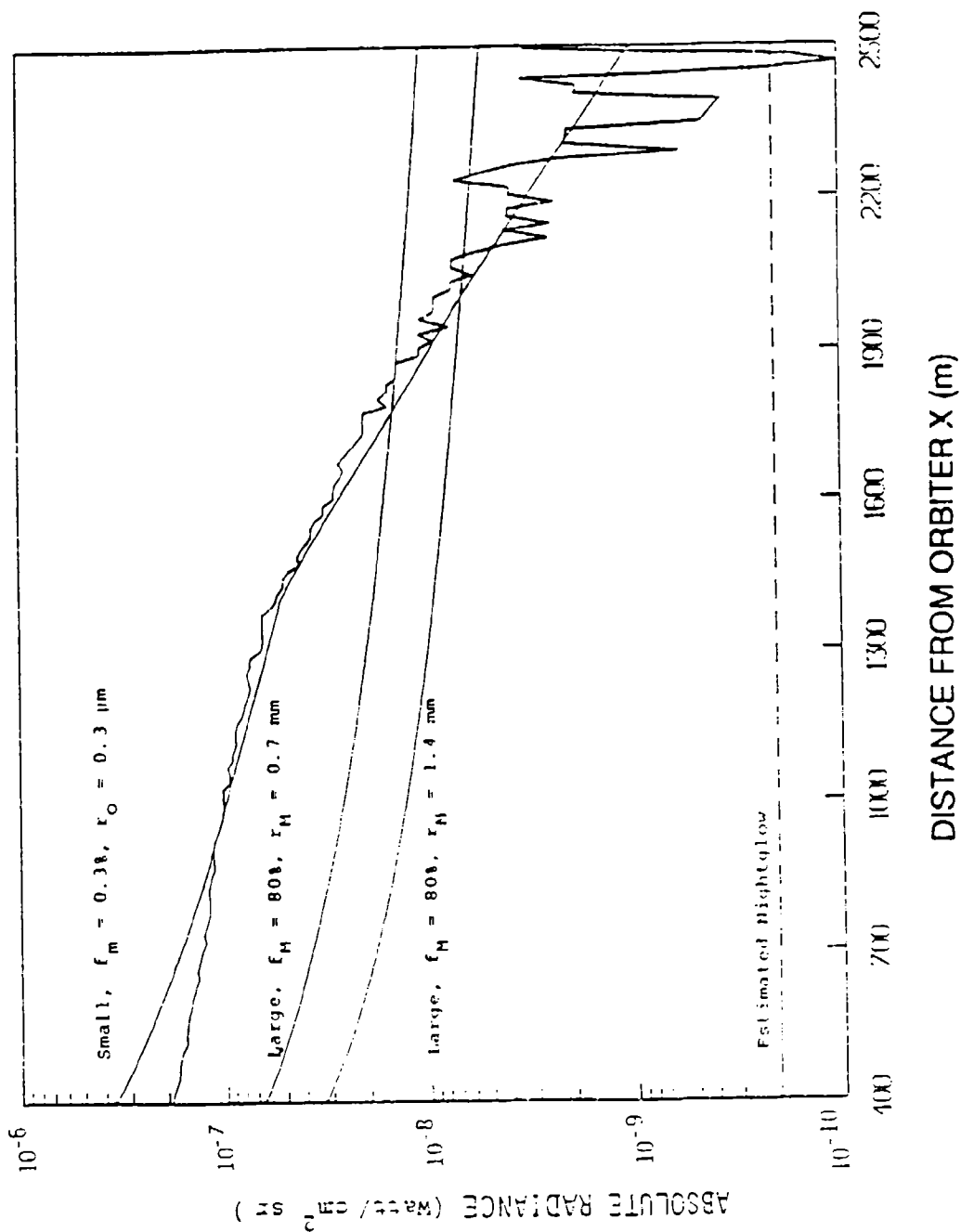


Figure 10. Calculated absolute axial radiances of the clouds of submicron- and ~mm-diameter particles in the projection to AMOS of Figures 2c and 4, for the particle radii and fractions of total vented water indicated. (Compare Figure 5.)



projection to AMOS. With the parameters of these particles identified by the subscript M, the ratio of radiances is

$$B_m/B_M = (f_m/f_M) (r_M/r_0)^3 [(dC_{SC}/d\Omega)_m(X)/(dC_{SC}/d\Omega)_M]. \quad (7)$$

( $r_M$  of course represents an average over the broad size distribution, as does the scattering cross-section.) Equation (7) explicitly includes the dependence on  $X$  of the differential scattering cross-section of the sublimating submicron particles; in contrast the corresponding term for the large particles stays about constant, since the relative decrease in the average "radius" of these particles is small (Appendix C). In consequence the dependence of  $B_M$  on  $X$  reduces to the  $1/X$  ( $\equiv$  [sight path  $X$ ]/[divergence  $X^2$ ]) factor--compare Equation (6) --, as is shown in Figure 10 for the two mean (actually, assumed monodisperse) radii of the large particles.

Figures 5 and 10 present strong evidence that  $B_m/B_M$  is greater than 1 over the instrumentally-detectable length of the trail. Since signal-to-noise in the summed video image illustrated in Figure 2c and Figure 4 deteriorates rapidly beyond about 2 km from Orbiter, we adopt the bound

$$B_m/B_M \geq 1 \quad \text{at } X = 2 \text{ km.} \quad (8)$$

Equation (A11) gives  $r = 0.15 \mu\text{m}$  at this downstream distance [with  $r_0 = 0.3 \mu\text{m}$ ], for which  $(dC_{SC}/d\Omega)_m = 3.5 \times 10^{-11} \text{ cm}^2\text{sr}^{-1}$  at  $\eta_1 = 48^\circ$ ;  $(dC_{SC}/d\Omega)_M$  at the same sunlight scattering angle is  $0.1 \pi r_M^2 \text{ cm}^2\text{sr}^{-1}$  (Figure 9). With the fraction  $f_M$  of the vented water mass that becomes these large particles taken as 0.8 (Ref 2) and the other numerical values stated above, Equations (7) and (8) give

$$B_m/B_M = 3.5 \times 10^3 f_m r_M \geq 1 \quad \text{[in the AMOS image].} \quad (9)$$

We return to Equation (9) in the next subsection.

#### 10. Photometric Analysis of the Onboard-Camera Images

The discrete large ice particles are the dominant feature in the frames from the close-lying onboard cameras (Figures 1, 7, and 8), with some particles producing irradiances high enough to induce undershoots in the video output current. Overlying their instrumentally-blurred and -bloomed images is a spatially-continuous haze with sensibly the same transverse angular extent as the cloud of these distinguishable particles, part of which may be presumed to be due to scattering of sunlight from the submicron particles.

We calculated the irradiances at the focal plane of the aft bay camera due to scattering of direct sunlight from both size ice particles, neglecting the small contribution from solar photons that are first scattered off Discovery's body. The camera parameters adopted are focal length  $F = 1.3$  cm (derived from the calculated  $47\frac{1}{2}^\circ$  field of view and  $\frac{1}{2}$ -inch physical width of the photocathode), clear aperture  $A = 1$  cm<sup>2</sup> (as would apply to a lens with relative aperture  $f/1.5$ ;  $A$  in fact cancels out of the argument), and effective image blur spot  $A' = 40$   $\mu$ m  $\times$   $40$   $\mu$ m. (Our conclusions are not particularly sensitive to these camera characteristics.) The relevant scene-lighting parameters at the typical distance into the wake  $X \approx 20$  m are aspect angle  $\eta'_2 \approx 45^\circ$  and scattering angle  $\eta'_1 \approx 140^\circ$ . Thus for small-particle radius  $r = 0.3$   $\mu$ m the differential visible light scattering cross-section  $(dC'_{sc}/d\Omega)_m$  is  $1.4 \times 10^{-11}$  cm<sup>2</sup>sr<sup>-1</sup> (from Figure 9; the prime symbol refers to the projection to the onboard camera). The irradiance produced at the focal plane by the cloud of submicron particles is thus closely

$$I_m' = \pi B_m A / 4F^2, \quad (10)$$

with the surface brightness  $B_m$  given by the equivalent of Equation (6). Substitution of the numerical values gives

$$I_m' = 4.2 \times 10^{-5} f_m \text{ w/cm}^2. \quad [X = 20 \text{ m, bay camera}] \quad (11)$$

The sterance  $S_M$  of individual large ice particles is

$$S_M = I_{\text{sun}} (dC_{\text{sc}}'/d\Omega)_M \text{ w/sr.} \quad (12)$$

From Figure 9 we find that at  $\eta_1' \approx 140^\circ$ ,  $(dC_{\text{sc}}'/d\Omega)_M = 1 \times 10^{-2} \pi r_M^2$ . As these particles lie outside the hyperfocal distance of the bay camera's relatively short focal length lens, the corresponding irradiance at this camera's focal plane is then

$$I_M' = (S_M/R'^2) (A/A'). \quad (13)$$

With  $R' \approx 30 \text{ m}$  adopted as the range to the onboard camera of the single sunlight-scattering particle located at  $X = 20 \text{ m}$ ,

$$I_M' = 6.5 \times 10^{-6} r_M^2 \text{ w/cm}^2. \quad [\text{bay camera}] \quad (14)$$

The ratio of irradiances at the image plane from scattering of sunlight by the relatively-few discrete large particles (still approximating them as spherical) and by the optically-continuous cloud of many smaller particles (also assumed spherical, despite their surface roughening) is then

$$I_m'/I_M' = 6.4 f_m/r_M^2. \quad (15)$$

(A more detailed analysis shows this ratio to be about 20% lower for "bowl-shaped" large ice particles.) This ratio is independent of the solar irradiance and the clear aperture  $A$  of the camera lens (although, of course, not of the solar-scatter angle  $\eta_1'$ ). The quantitative statement of the observation that the large particles stand out clearly in the images from the onboard video camera is

$$I_m'/I_M' (= 6.4 f_m/r_M^2) < 1. \quad (16)$$

## 11. Particle Parameters

From the constraint expressed by the inequalities of Equations (9) and (16) and the estimated number density of the distinguishable large particles, we can determine the mass fraction  $f_m$  in the small particle and mean radius  $r_M$  of the large particles. Figure 11 shows what we may term the f-r domain of the two-component cloud of ice particles, which bounds these two quantities from the observed ratios of radiance toward AMOS from  $X > \sim 600$  m and of irradiance at Discovery's bay camera from  $\sim 5$  m  $< X < \sim 100$  m. The number of large scattering particles per unit length of trail seen in bay camera video frames such as shown in Figure 8 is as noted previously  $100 \pm 50 \text{ m}^{-1}$  (this figure includes a small allowance for particles obscured by overlap near the axis of the trail). From the known water venting rate  $dM'/dt$ , mass fraction in large particles  $f_M$ , and measured particle velocity  $v$ , we find that this particle density gives

$$r_M = 0.13 \pm 0.02 \text{ cm.} \quad (17)$$

This is of course an "average" radius, as the solar-scatter irradiances from individual large--and in all probability far from spherical--ice particles at fixed ranges from the bay camera show substantial variability. (Our neglect of the decrease in volume that results from sublimation as the initially  $\sim 330\text{K}$  liquid water droplets cool, freeze, and then cool further is justified in Appendix C.)

Applying this mean figure to the constraints illustrated in Figure 11, we find

$$f_m \sim 0.2 - 0.35\%, \quad (18)$$

in effect the fraction that we used earlier.

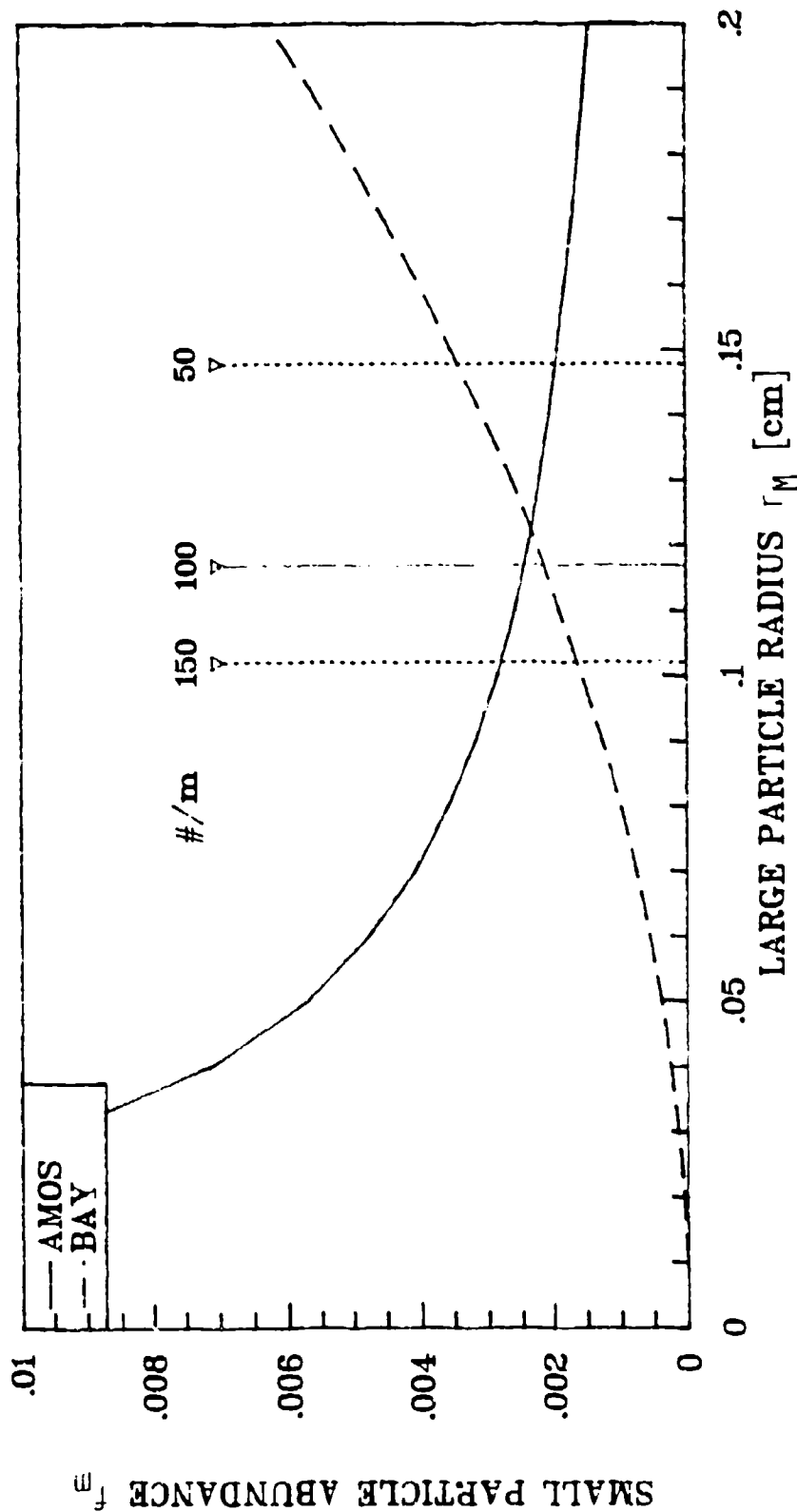


Figure 11. Small particle abundance-large particle size ( $f$ - $r$ ) diagram of the STS-29 water stream. The decreasing curve, which bounds  $f_m > 4.6 \times 10^{-4} r_M^{-1}$  [Equation (9)], results from the observation that the groundbased signal is dominated by scattering of sunlight from the small particles. The increasing curve, which bounds  $f_m < r_M^2$  [Equation (16)], results from the observation that the large particles dominate in the projection to the onboard camera. The mean large-particle radius  $r_M = 0.13 \pm 0.02$  cm [Equation (18)] is obtained from the "measured" number of discrete scatterers per unit trail length.

The errors stated in Equations (17) and (18) take account only of the uncertainty in the number of large particles per unit length of trail; while the total uncertainty in  $r_m$  (an average, and in fact poorly defined) and  $f_m$  is expected to be higher, this uncertainty is in all probability less than  $\pm 50\%$ .

#### 12. Radiation and Scattering at Other Wavelengths

In Appendix D we estimate axial radiances in the infrared of the water trail at 1 m and 1000 m from the venting nozzle. This thermal emission comes principally from the large ice particles, as the rapidly-evaporating small particles are very inefficient IR radiators; that is, the ratio of brightnesses is the reverse of that from scattering of visible sunlight. When the droplet temperatures become lower than that of the earth-and-atmosphere, the trail actually exhibits "negative contrast" in nadir-directed projections; nonetheless its thermal infrared brightnesses are large compared with the earth's limb above the mesosphere (refer to Appendix D for details).

#### 13. Contamination of Orbiter

As we have noted above, the video images do not resolve the unrecondensed water gas, nor do the optical data confirm the prediction of the fraction of vented water that becomes vaporized directly or locate the origin of this gas (beyond showing where the coherent liquid stream fragments into the large droplets). In consequence we have chosen not to address here the issues of transport of this gaseous contaminant back to Shuttle Orbiter, or of the infrared (Ref's 13, 14) and some visible (Ref's 14, 15) emissions excited when these  $\sim 8$  km/s translational velocity water molecules collide with the atmosphere (other than a brief mention in Table D1, in the interest of completeness). The mean free path of water molecules at Discovery's orbital altitude is of the order of 10 km.

The video images show no evidence that any of the fragmentation-product and recondensation water/ice particles flow

backward in the frame of reference of the orbiting spacecraft to recontact its body (although the large ice droplets, in some posigrade trajectories, are sufficiently longlived to collide with it on subsequent orbits; see Ref 5.)

#### 14. Conclusions

Table 1 summarizes the numerical results of our analysis of the groundbased and onboard intensified-video images of the sunlit space shuttle supply water that was vented into the wake of Discovery on STS Mission 29. The data lead to the following principal interpretations of the phenomenology of narrow liquid streams in the near-vacuum and radiation environment of low earth orbit, which appear to be at least qualitatively consistent with laboratory-tank simulations.

1) The high vapor pressure liquid forms into ice particles with two size components: submicron-diameter droplets from recondensation of the rapidly-evolved gas, whose radiance dominates the images from the distant AMOS telescope-camera; and irregular, polydisperse particles produced in its initial cavitation rupturing (or flash evaporation) with mean "diameter" somewhat larger than that of the vehicle nozzle, many of which can be followed in the video photographs from the much more closely located spacecraft cameras. The water that vaporizes from the surfaces of the coherent stream and large water/ice droplets (from straightforward thermodynamic arguments, 20% plus a few percent more while the ice particles cool by sublimation to an equilibrium daytime temperature) is not detectable by these optical sensors; it is manifested only by its partial condensation into the small ice particles when this gas has become overexpanded.

2) The angular spreads of the two types of particle are the same within experimental uncertainty; the small ( $\pm \sim 15^\circ$ ) divergence shows that the energy imparted to the liquid by unbalanced surface tension forces when the enclosed expanding steam bubbles break through the surface is substantially less

Table 1. Summary of Results from the Photometric/Photogrammetric Analysis of the Groundbased and Onboard Images of the Trail of Ice Particles Produced by Water Vented from Space Shuttle on Mission STS-29.

<u>QUANTITY</u>	<u>DERIVED VALUE</u>	<u>COMMENT</u>
Longitudinal Particle Velocity	$v = 23 \text{ m/s}$ $+6, -8 \text{ m/s}$	Both flow components; indistinguishable from the liquid stream velocity
Transverse Particle Velocity	5 m/s nominal average	Both flow components; little kinetic energy is imparted by the cavitation explosion of the stream
Small-particle Radius	$r_o = 0.3 \mu\text{m} \pm 50\%$ initially	Compatible with laboratory simulation results; decreases with distance along the trail [Eq (A11)].
Small-particle Abundance	$f_m = 0.3\% \pm 50\%$ of initial water vented	Eq (19); derived from constraint from image-plane irradiances at two camera distances
Large-particle Abundance	$f_M = 80\%$	Adopted, from thermodynamic arguments
Large-particle Radius	$r_M = 0.13 \text{ cm}$ $\pm 25\% \text{ (mean)}$	Eq (18); average figure, about twice nozzle radius; compatible with simulation
Small-particle Cloud Brightness 0.4-0.6 $\mu\text{m}$ ( $\eta_1 = 48^\circ, \eta_2 = 33^\circ$ , at $X = 1 \text{ km}$ )	$B_m = 1 \times 10^{-7}$ $\text{w/cm}^2 \text{ sr}$	Figure 10; from $f_m$ and $r_o$ , no absolute calibration is available but could be checked against irradiance from a known star
Large-particle Cloud Brightness (same viewing conditions)	$B_M < B_m/-10$	Figure 10
Night sky brightness 0.4 to 0.6 $\mu\text{m}$ ( $\eta_3 = 60^\circ$ )	$2 \times 10^{-10}$ $\text{w/cm}^2 \text{ sr}$	Nominal figure, much lower than baseline and hence the scene backgrounds are most likely instrumental
Infrared cloud radiance (Axial-perpendicular projection at $X = 1 \text{ km}$ )	$10^{-13} \text{ w/cm}^2 \text{ sr}$ 3-5 $\mu\text{m}$ $10^{-10} \text{ w/cm}^2 \text{ sr}$ 8-12 $\mu\text{m}$ $10^{-13} \text{ w/cm}^2 \text{ sr cm}^{-1}$ 11 $\mu\text{m}$ ( $\times 10^{-5}$ at $X = 1 \text{ m}$ )	Due to blackbody thermal radiation from the large particles



than the kinetic energy with which it is vented; and the longitudinal velocities of the large particles are indistinguishable from that of the initial water stream (which appears to achieve Poiseuille flow within the conical venting nozzle) and furthermore vary very little among themselves.

3) The submicron particles--initially, very "efficient" scattering centers--sublimate in the solar and thermal earthshine radiation field to below the AMOS camera's optical threshold ( $\sim 10^{-8}$  w/cm<sup>2</sup> sr) within about 2 minutes, at rates predictable by standard Mie scattering/absorption theory when a small correction is applied for the progressive roughening of their outer surfaces (as in Appendix A). These particles, whose energy budget is calculated approximating their shapes as spherical, become "Rayleigh" scatterers-- $2\pi r/\lambda \ll 1$ --about halfway along the trajectories detectable above camera noise in the groundbased images (see Figure 10). They reach an equilibrium temperature of 166K in  $\sim 1$  s, while the more infrared earthshine-absorbing and initially non-isothermal large particles cool to about 180K in  $\sim 100$  s; refer to Figures B2 and C1.

4) The relative irradiances from the two types of particle in the two projections and the number of large particles estimated from counting individual bright moving spots in the onboard images impose a joint constraint on the fraction of the vented water in submicron droplets and the mean radius of the  $\sim$ mm-diameter droplets. (In contrast to the small ice particles, the large particles undergo a small fractional change in volume over their observable trajectory; see Appendix C.) The best-estimate mass fraction of small particles is 0.3%, which is about 1% of the initially-vaporized water or "steam"; and the average radius of the large particles is 1.3 mm, with the relatively broad distribution also seen in laboratory simulations indicated by the variability of the irradiances from particles at the same range from the bay onboard camera.

5) The radiances of the release trail at infrared wavelengths are due principally to thermal emission from the

(essentially-blackbody, albeit cold) large particles. At 1 km from the venting nozzle these radiances are comparable with that of the earth limb at -100 km in the long wavelength-infrared "window" (as derived in Appendix D).

The arguments from which this quantitative information is derived apply the assumption that the droplets are both spherical and (bimodally) monodisperse, which undoubtedly introduces some error. The large sunlit ice particles in fact are seen to flicker--which we interpret as tumbling of nonspherical shapes--, as well as to vary in size--as would be expected of the products of an uncontrolled rupturing that are subject to further distortion and even fracturing in the freezing process (Ref 6). In contrast the small particles undergo transition to the essentially-Rayleigh scattering regime over a short distance along their wake path, which indicates both a narrow initial size distribution and a moderate effect of the roughening up to this downstream distance (as would also be expected: the sublimation "instability" leads to an increasing rate of alteration of the surface).

We note again that none of the large ice particles can be seen streaming backward (in Orbiter's frame of reference) to strike the spacecraft body, and as the submicron droplets show every evidence of moving with these large particles they would also not recontact outer surfaces of the vehicle. However much of the vapor evolves from the coherent stream and large droplets within an outboard distance small compared with Orbiter's dimensions (Appendix C; see also Ref 4), and the mean thermal speed of this gas is considerably greater than the venting velocity; in consequence some fraction of the ejected liquid directly returns to contaminate the spacecraft, and further initially-retrograde water molecules scatter back off the residual atmosphere into its path. (This return flux of water vapor is not calculated here, as the video data analyzed provide no new direct information on this issue.)

## Appendix A

### SUBLIMATION FROM SUBMICRON-DIAMETER ICE PARTICLES IN THE LOW EARTH-ORBITAL ENVIRONMENT

#### Theoretical Background

The small ice particles formed from recondensation of water vapor in low-altitude orbits rapidly cool (Appendix B) and lose volume by sublimating into the surrounding quasi-vacuum. Their daytime energy budget is made up of three terms: absorption of direct sunlight (principally, in the short-wavelength infrared) and incident earthshine (at somewhat longer wavelengths); thermal re-radiation (at still longer average wavelengths); and the heat loss due to this sublimation. (Heating by scattered sunlight can be neglected because the atmosphere's water vapor absorbs over sensibly the same spectral regions as solid water; and heating by aerodynamic collisions is very small above 300 km altitude when the particle radius exceeds about 10 Å.)

The rate of change of temperature  $dT/dt$  of spherical ice particles with radius  $r$  can therefore be written (compare Ref's 12 and 16)

$$\begin{aligned} \frac{4\pi}{3}r^3\rho C \frac{dT}{dt} = & [\int \epsilon(r,\nu)\Omega_e r^2 q_e(\nu) d\nu + \int \epsilon(r,\nu)\Omega_s r^2 q_s(\nu) d\nu] \\ & - \int \epsilon(r,\nu)\Omega_p r^2 B(\nu,T) d\nu + 4\pi r^2 \rho L \frac{dr}{dt}. \end{aligned} \quad (A1)$$

Here

- $\rho$  = density of ice = 0.92 g/cm<sup>3</sup>
- $C$  = average specific heat of ice between 250K (the approximate droplet formation temperature; see Ref 6) and 160K = 1.9 J/gK° (= 0.45 cal/gK°)
- $L$  = average heat of sublimation of ice over this temperature range =  $2.8 \times 10^3$  J/g
- $\nu$  = wavenumber of emitted/absorbed electromagnetic radiation

- $\epsilon(r, \nu)$  = particle emissivity ("effective" emissivities are defined below)  
 $B(\nu, T)$  = Planck radiation function ( $c$ ,  $k$ , and  $h$  have their conventional meanings) =  $2hc^{-2}\nu^3(e^{h\nu/kT}-1)^{-1}$   
 $q_e$  =  $B(\nu, T_e = 280K)$ , for the earth approximated as a 280K blackbody  
 $q_s$  =  $B(\nu, T_s = 5800K)$ , for the sun approximated as a 5800K blackbody  
 $\Omega_e$  = solid angle subtended by the earth at the 329-km altitude particle  $\approx 1.4\pi$  sr  
 $\Omega_s$  = solid angle subtended by the sun at the particle =  $6.8 \times 10^{-5}$  sr  
 $\Omega_p$  = solid angle into which the particle radiates (isotropically) =  $4\pi$  sr.

In Appendix B we solve this equation to show that submicron-radius ice droplets orbiting at 329 km asymptotically approach an equilibrium temperature of 166K in  $<-1$  s, which is roughly 20 m path at their about-20 m/s longitudinal velocity relative to the spacecraft (or 10 km in the static atmosphere). Thus the sunlight-scatter brightnesses of the trail beyond this separation result from particles at a steady-state temperature, whose cooling by sublimation (last term in Equation (A1)) is balanced by their net absorption of radiation (first three terms). (At shorter ranges from Orbiter--and indeed, to even considerably longer ranges--the AMOS video signal is dominated by blooming of the irradiances from the spacecraft's body; the sunlight-scatter radiances in this region can be calculated following the procedure applied here.)

Computations applying standard Mie theory with the complex index of refraction of ice (at 266K), have resulted in the wavelength- and radius-dependent emissivity of spheres shown in Figure A1 (Ref 17). Most of the heating of submicron particles is from infrared earthshine. We computed for input to our later calculations "effective" emissivities at  $r = 0.2 \mu\text{m}$  for

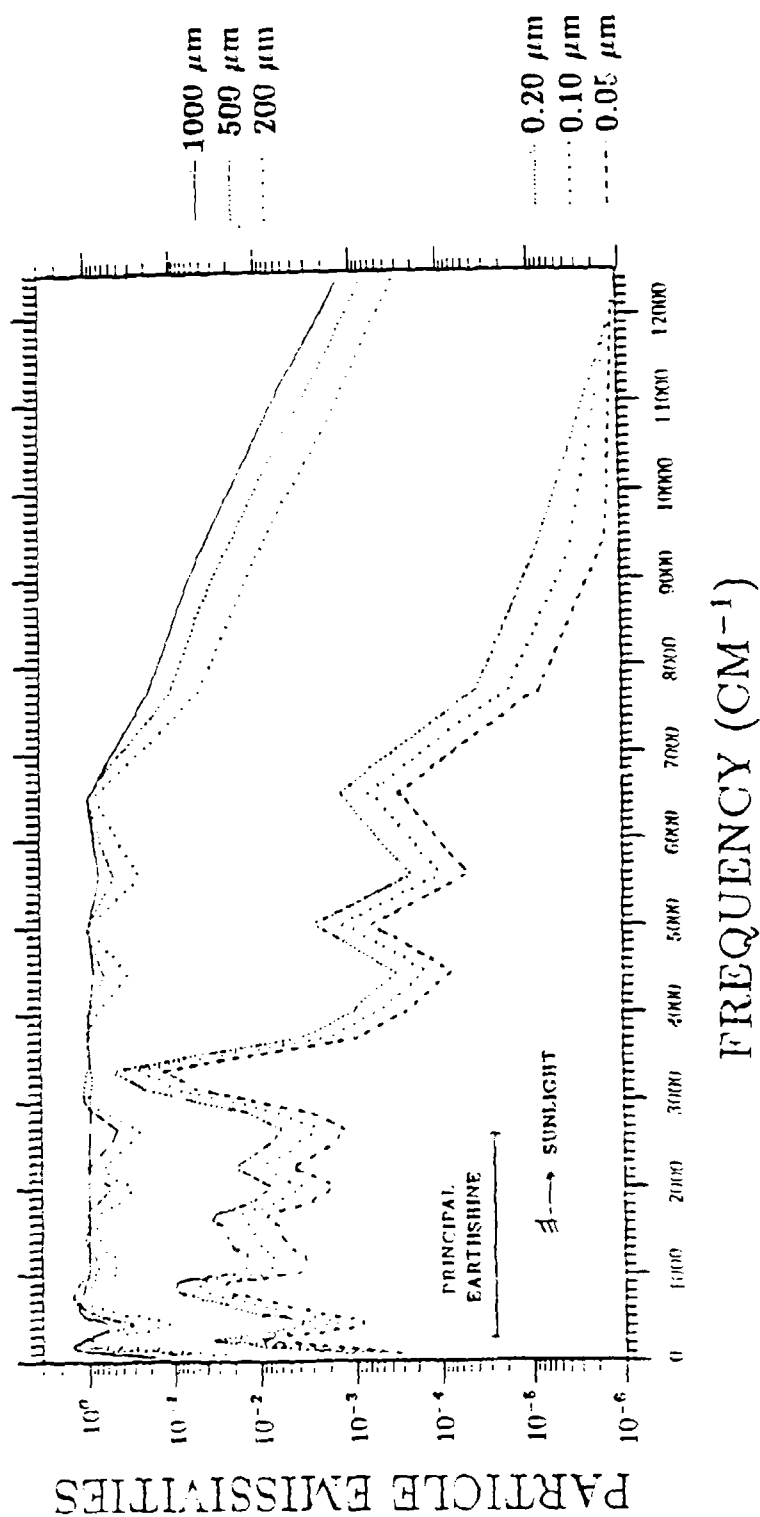


Figure A1. Emissivity of large and small spherical ice particles of the radii indicated at right, calculated from the complex index of refraction at 266K in Ref 17. The spectral irradiance of sunlight ( $\text{per cm}^{-1}$ ) varies by only one order of magnitude above 1600  $\text{cm}^{-1}$ .

earthshine ( $\epsilon_e$ ), for the particle's thermal radiation ( $\epsilon_p$ ), and for sunlight ( $\epsilon_s$ ) by weighting and averaging these calculated emissivities over each blackbody distribution function at its radiating temperature, getting  $2.0 \times 10^{-2}$ ,  $2.2 \times 10^{-2}$ , and  $0.25 \times 10^{-2}$  respectively.

#### Particle Radius Calculations

These effective emissivities lead directly to an estimation of the steady-state sublimation rate. Equation (A1) becomes

$$dr/dt = (-\sigma/4\pi\rho L) \cdot (\epsilon_e \Omega_e T_e^4 + \epsilon_s \Omega_s T_s^4 - \epsilon_p \Omega_p T^4), \quad (A2)$$

where  $\sigma = 5.7 \times 10^{-12} \text{ Js}^{-1}\text{cm}^{-2}\text{K}^{-4}$  is the Stefan-Boltzmann constant. With substitution of the parameters listed above,

$$dr/dt = -1 \times 10^{-4} (12 + 4 - 8) = -8 \times 10^{-4} \mu\text{m/s},$$

which is consistent with the more precise result (from our graphical solution in Appendix B) in Figure B3.

When  $r$  is between  $10^{-2} \mu\text{m}$  and  $1 \mu\text{m}$  it decreases exponentially with time, that is, with distance from Orbiter's water-venting nozzle. This dependence stems from the fact that the spectral emissivity of weakly-absorbing spheres is proportional to  $r$  when the particle circumference  $2\pi r$  lies in the range between small compared with and somewhat larger than the photon wavelength. (For the exact conditions under which this proportionality obtains, see for example Ref 18, Chapters 5 and 7.) The arguments in Section 8 of the main text show that the radiances measured at AMOS (as in Figures 4, 5, and 6) are due principally to scattering of sunlight from ice particles in this size range. The ("mean") radius of these particles at time  $t$  after they form is then

$$r = r_0 e^{-t/\tau}, \quad 10^{-2} \mu\text{m} < r < 1 \mu\text{m} \quad (A3)$$

where  $r_0$  is their initial radius and  $r^{-1} = dr/rdt$  their fractional sublimation rate. From Figure B3, we find that these submicron particles lose  $(1 - 1/e)$  of their radius and thus 95% of their mass in  $\tau = 222$  s.

With  $v$  the (constant) axial velocity of these particles and  $X$  the axial distance from the nozzle,

$$r = r_0 e^{-X/v\tau} \equiv r_0 e^{-X/D}. \quad 10^{-2} \mu\text{m} < r < 1 \mu\text{m} \quad (\text{A4})$$

Since  $v = 20$  m/s (to one significant figure), the e-folding distance of particle radius  $D \equiv v\tau$  would be  $4\frac{1}{2}$  km.

#### Calculations of the Trail Radiance

The differential scattering cross section  $dC_{sc}/d\Omega$  of weakly-absorbing particles is known from classical Rayleigh-Mie theory to vary as  $r^2$  in the limit of particle circumference  $2\pi r$  large compared with the photon wavelength, and as  $r^6$  ( $= r^2 \cdot r^4$ ) in the opposite limit. We therefore apply the approximation

$$(a) \quad dC_{sc}/d\Omega \sim r^2, \quad r \geq 0.15 \mu\text{m} \quad (\text{A5})$$

$$(b) \quad dC_{sc}/d\Omega \sim r^6, \quad r < 0.15 \mu\text{m} \quad (\text{A6})$$

where (a) may be termed the "geometric" scattering region and (b) the Rayleigh region. The sharp transition adopted ignores the familiar Mie oscillations in the cross-section, since (as also noted in Section 8) these would be largely washed out by the polychromatic solar illumination and relatively broad spectral sensitivity of the AMOS camera; the radius  $r = 0.15 \mu\text{m}$  at which transition takes place is appropriate for the sunlight spectrum and  $0.4 - 0.65 \mu\text{m}$  FWHM photon response of S-20R photocathodes.

Should the sublimating recondensation particles be initially formed with  $r_0$  somewhat larger than  $0.15 \mu\text{m}$ , they would at first scatter sunlight photons in the geometric regime (a), and then later after  $r$  has decreased in the Rayleigh regime (b).

Equations (A4) - (A6) show that the brightnesses measured at AMOS

in individual video frames, summed in the direction perpendicular to the longitudinal axis of the trail, would vary as

$$(a) \quad e^{-2X/D}, \quad X \leq X_1 \quad (A7)$$

$$(b) \quad e^{-6X/D}, \quad X > X_1 \quad (A8)$$

where  $X_1$  is the boundary between the two regions/regimes. This transverse spatial integration removes the effect of divergence of the particle beam, as it represents the total differential scattering cross-section per unit path remaining at longitudinal distance  $X$ . Equations (A7) and (A8) show that over a short transition length the e-folding distance of this integrated radiance would change by a factor 3, from (radius e-folding distance  $D$ )/2 = 2.2 km to  $D/6 = 0.75$  km.

Figure 5b is a plot of these summed-brightnesses measured from the 61° zenith angle projection as described in the text. A transition near 1.4 km is apparent, with the e-folding distances about 1.7 km and 0.4 km in the two segments. Both these scale lengths are smaller than we predicted immediately above for smooth ice spheres, the discrepancy being greater (almost a factor 2) where  $X > 1.4$  km (region (b)). Furthermore--and as also pointed out in Section 8-- , closer examination of Figure 5 shows that the characteristic lengths of both the axial (Figure 5a) and crosswise-summed brightnesses are decreasing with distance from the volume where the small ice particles are formed, with the curvature more pronounced in region (b).

#### Surface Roughening

These photometric data indicate, then, that

- 1) The actual sublimation rate of submicron ice droplets is higher, by factors up to about 2, than our classical calculations predict; and
- 2) the rate must be monotonically increasing with distance (or time) along the wake trail.



Laboratory experiments (Ref 12) have shown that the initially smooth surfaces of ice droplets sublimating in vacuum gradually roughen, leading to enhanced mass loss rates. The effect is ascribed to an increase in the imaginary component of the index of refraction (the result of a multiphonon process), which increases the absorption of optical radiations, rather than to a gross increase in the exposed surface area. Extrapolation from Figure 16 of Ref 12 (in which much larger particles-- $r_0 > 40 \mu\text{m}$ --are considered) indicates agreement with the two observations above:

- 1) a factor-two increase in the sublimation rate of ice particles whose mean diameter has decreased to  $< \frac{1}{2} \mu\text{m}$  is physically reasonable; and
- 2) this relative enhancement itself progressively increases as the particle size decreases.

Surface roughening--due to spatially-irregular sublimation--thus provides a natural explanation for the gradually-increasing rates at which the sunlight scattering intensities decrease in Figure 5.

A simple model of this enhanced sublimation follows from assigning to  $\tau$  a weak dependence on  $X$  (or  $t$ ). Redefining  $\tau^{-1} \equiv \alpha$  as the fractional rate at which the rough particle's "radius"  $r$  decreases by sublimation, we take  $\alpha$  to be a monotonically increasing function whose Taylor series expansion is

$$\alpha(t) = \alpha_0 + \alpha_1 t + \alpha_2 t^2 \dots \quad (\text{A9})$$

(This approach is mathematically equivalent to that which would result from expanding the exponential increase in imaginary index of refraction with the [increasing] roughness parameter  $S$  in Equation (50) of Ref 12.)  $\alpha_0 \equiv \alpha(t = 0)$  is the initial fractional radius-sublimation rate, and  $\alpha_1 > 0$ .

If the ice droplets initially formed by recondensation close to the water release nozzle are reasonably smooth,  $\alpha_0$  would be near the aforementioned value in Figure B3:

$$\alpha_0 \approx \tau^{-1} = 4.5 \times 10^{-3} \text{ s}^{-1}. \quad (\text{A10})$$

Truncating the expansion in Equation (A9) at the second term is equivalent to making  $\alpha$  increase linearly with pathlength or time, which is a reasonable first approximation (in particular since the second term in the expansion of Ref 12's exponential increase in absorption coefficient would also be proportional to  $t$ ).

Equation (A4) now becomes

$$r = r_0 e^{-(\beta_0 + \beta_1 X)X}, \quad (\text{A11})$$

where

$$\beta_0 \equiv \alpha_0/v, \quad \beta_1 \equiv \alpha_1/v^2. \quad (\text{A12})$$

Similarly, the transverse-integrated radiances in the two sunlight-scattering regions become

$$(a) \quad e^{-2(\beta_0 + \beta_1 X)X}, \quad X \leq X_1 \quad (\text{A13})$$

$$(b) \quad e^{-6(\beta_0 + \beta_1 X)X}, \quad X > X_1. \quad (\text{A14})$$

The solid lines in Figure 5 fit Equations (A13) and (A14) to the photometric data with  $\beta_0 = 2.0 \times 10^{-4} \text{ m}^{-1}$  and  $\beta_1 = 8.0 \times 10^{-8} \text{ m}^{-2}$  ( $= \beta_0/2500 \text{ m}$ ). Thus  $\alpha_0 = 4.5 \times 10^{-3} \text{ s}^{-1}$  (as in Equation A10) and  $\alpha_1 \approx 3 \times 10^{-5} \text{ s}^{-2}$ .

### Conclusions

The radiance decay parameter  $\alpha(t)$  increases linearly [in our model] from  $\alpha_0 = 4\frac{1}{2} \times 10^{-3} \text{ s}^{-1}$  to  $2\alpha_0$  at 125 s, that is, at  $2\frac{1}{2} \text{ km}$  where the ice-particle trail is no longer detectable by the AMOS camera. This maximum factor-2 increase in the characteristic fractional sublimation rate of "old" and therefore highly-irregular droplets is well within physical reason. The numerical value of  $\alpha_0$  obtained from the fit to the groundbased video data suggests that the ice particles initially formed by

recondensation of the overexpanded water gas have relatively smooth surfaces.

Substitution of  $r = 0.15 \mu\text{m}$  at  $X_1 = 1.4 \text{ km}$  in Equation (A11) with the values  $\beta_0$  and  $\beta_1$  stated just above yields  $r_0 = 0.23 \mu\text{m}$  as the mean radius of the ice particles upon formation. Since the geometric-to-Rayleigh transition is not sharply defined even for monochromatic light, we estimate the actual initial mean radius  $r_0$  of the recondensation particles to lie between  $0.2 \mu\text{m}$  and  $0.35 \mu\text{m}$ , the "best-estimate" being  $0.3 \mu\text{m}$ .

In summary, a heuristic model of progressive surface roughening incorporated into our approximated geometric-then-Rayleigh scattering of sunlight by quasispherical submicron ice particles sublimating in the low-earth orbital environment provides a quantitative explanation of the rates of decrease of total radiance from the vented-water trail that were measured by the AMOS video camera.

## Appendix B

### TEMPERATURE HISTORY OF THE SUBMICRON ICE PARTICLES

#### Background

We calculate here the dependence of temperature and radius of the initially-smooth, sublimating small recondensation particles considered in Appendix A on time after they are formed.

Equations (A1) and (A2) can be written as (dots denote time derivatives)

$$\frac{4\pi}{3} r \rho C \dot{T} - 4\pi r L \dot{r} = \epsilon_e \Omega_e \sigma T_e^4 + \epsilon_s \Omega_s \sigma T_s^4 - \epsilon_p \Omega_p \sigma T^4. \quad (B1)$$

We take the initial radius  $r_0$  as  $0.2 \mu\text{m}$  (the "mean" result from Appendix A), and an initial temperature  $T_0$  of the recondensed water vapor from the phase diagram of  $\text{H}_2\text{O}$  reproduced in Ref 6 as 250K. The exact value of  $T_0$  is not critical, as it does not affect the final equilibrium temperature and has only a negligible effect on the time to approach this equilibrium; the small variations with temperature in the specific heat  $C$  and heat of sublimation  $L$  of ice (Figure B1) have only a second-order effect on the results of the calculation; and the temperature  $T$  can be considered uniform throughout the droplet, since the high thermal diffusivity of  $\sim 200\text{K}$  ice ensures equilibration within its small volume in times very much shorter than the decay time(s) that we will derive (this unfortunately is not the case for the  $\sim 1000$ -times larger explosion-product ice particles, as we will see in Appendix C).

The vapor pressure curves of liquid and solid water reproduced in Figure B1 provide insight into the cooling-freezing process, since the sublimation rates are proportional to this pressure (except at the very highest temperatures, where some of the collisional water gas recondenses on the large particles). At  $T > \sim 180\text{K}$  this rapid sublimation is the dominant energy loss

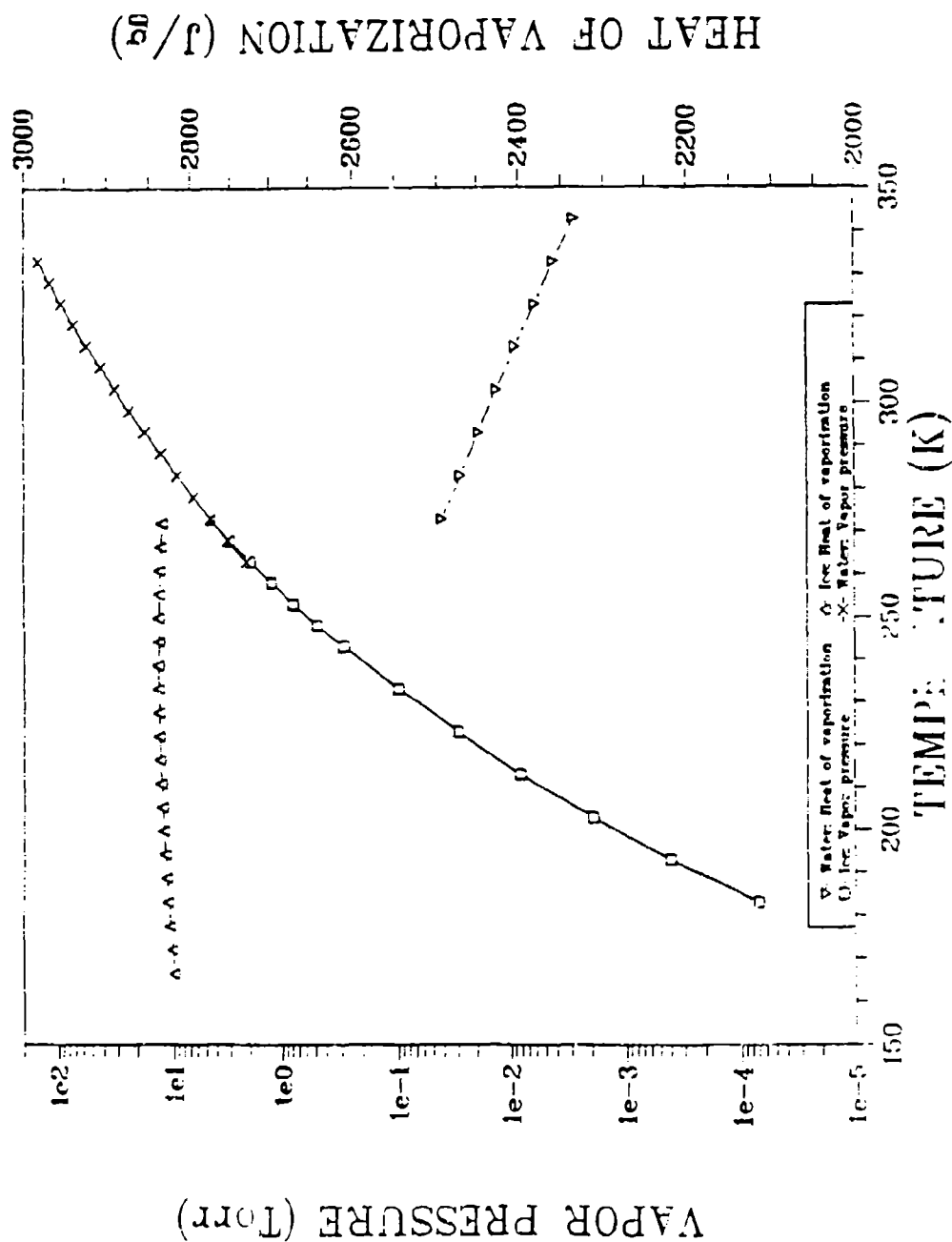


Figure B1. Vapor pressure and heat of vaporization of  $H_2O$ . A good fit to the vapor pressure curve is derived from an Arrhenius equation:

$$P \text{ (torr)} = 2.4 \times 10^{10} \exp (-6110/T)$$

mechanism, and then as the particles cool further the r-containing term decreases to values near those of the right hand side of Equation (B1); an asymptotic approach to a thermodynamic-equilibrium temperature is therefore expected. Substitution of the values of L and C given in Appendix A into the left-hand terms shows that the fractional decrease in radius per degree decrease in temperature is  $-1/4000$  during this period of sublimation dominance, and therefore a decrease in temperature from 250K to near 200K expends only about 2% of the initial droplet radius.

### Calculation

As pointed out in Appendix A, the emissivities of these weakly-absorbing submicron particles are proportional to their radius:

$$\epsilon_i = k_i r \quad (B2)$$

where i represents e, s, or p in the notation of Appendix A. From the numerical values of effective emissivity,  $k_e \approx 1.0 \times 10^3 \text{ cm}^{-1}$ ,  $k_p \approx 1.1 \times 10^3 \text{ cm}^{-1}$ ,  $k_s \approx 0.13 \times 10^3 \text{ cm}^{-1}$ . Substitution of (B2) into (B1) gives

$$r\dot{T} - \xi\dot{r} = \gamma r - \delta r T^4, \quad (B3)$$

where

$$\begin{aligned} \xi &\equiv 3L/C \\ \gamma &\equiv (3\sigma/4\pi\rho C) \cdot (k_e\Omega_e T_e^4 + k_s\Omega_s T_s^4) \\ \delta &\equiv 3\sigma k_p/\rho C \end{aligned} \quad (B4)$$

are constants.

To arrive at a unique solution to nonlinear differential equation (B3), another relationship between particle radius and temperature must be developed. The analysis of Ref 12 indicates that the rate of sublimation from the particles depends on their

vapor pressure, which displays a strong exponential (Arrhenius) dependence on surface temperature as illustrated in Figure B1. It can readily be shown that the ambient pressure at the surfaces of <250K submicron ice particles is so low that molecules leaving the surface have very low probability of returning, since their collisional mean free path in this gas is larger than the particle diameter. Under this condition the sublimation rate becomes (Ref 4)

$$\dot{r} = 0.27 P(T)/T^{1/2}, \quad (B5)$$

where  $P$  is the equilibrium vapor pressure in Torr for the particle surface temperature  $T$  and the units of  $r$  remain cm.

Equations (B3) and (B5) represent a complete set of coupled nonlinear differential equations, which we have solved numerically. We took the initial conditions for the ice particle as  $r_0 = 0.2 \mu\text{m}$  and  $T_0 = 250\text{K}$ , as mentioned above. We then followed the time dependence of  $r$  and  $T$  by using small linear steps in temperature (0.1K) until  $dT/dt$  for the next step became positive, after which we successively halved the temperature step until  $dT/dt$  after the next step returned to a negative value (the expected physical behavior: the particle temperature decreases monotonically, without oscillating).

Results of the numerical integration are shown in Figure B2. The particle cools by sublimation to 170K within 1/10 seconds. After about 1 s it has in effect reached its asymptotic temperature and fractional loss radius rate,  $T_{\text{eq}} = 166\text{K}$  and  $ur/rdt = 4.5 \times 10^{-3} \text{ s}^{-1}$ .

These results agree with those of a graphical solution shown in Figure B3, as well as with the "steady-state" sublimation rate that we calculated from Equation (A2). At equilibrium the  $\dot{T}$  term in Equation (B3) is zero, so that the equation can be solved for  $T(r)$ . This relationship is illustrated in Figure B3 as a function of particle size, along with the sublimation rate given

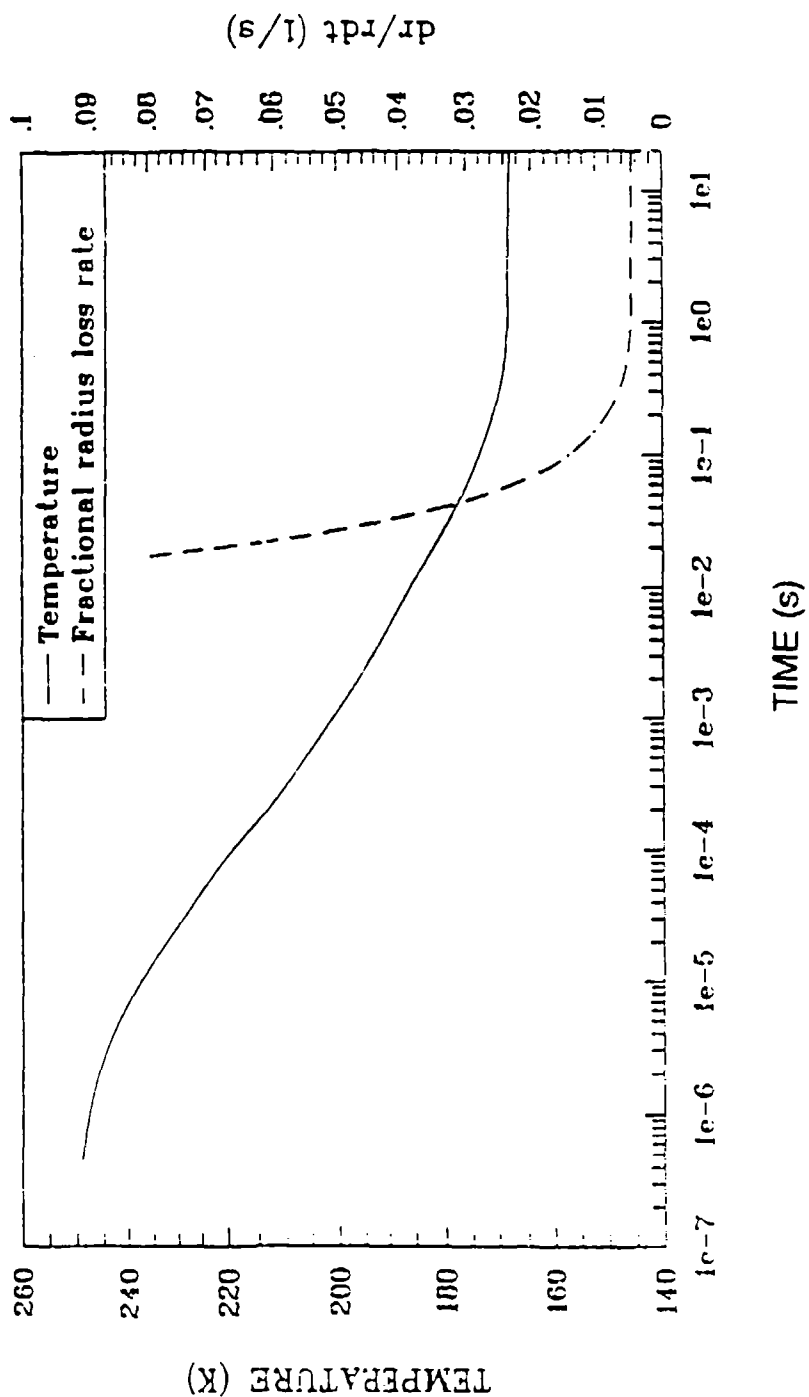


Figure B2. Temperature history of the submicron ice particles. The loss rate for the particle fractional radius approaches the value  $4.5 \times 10^{-3} s^{-1}$ .



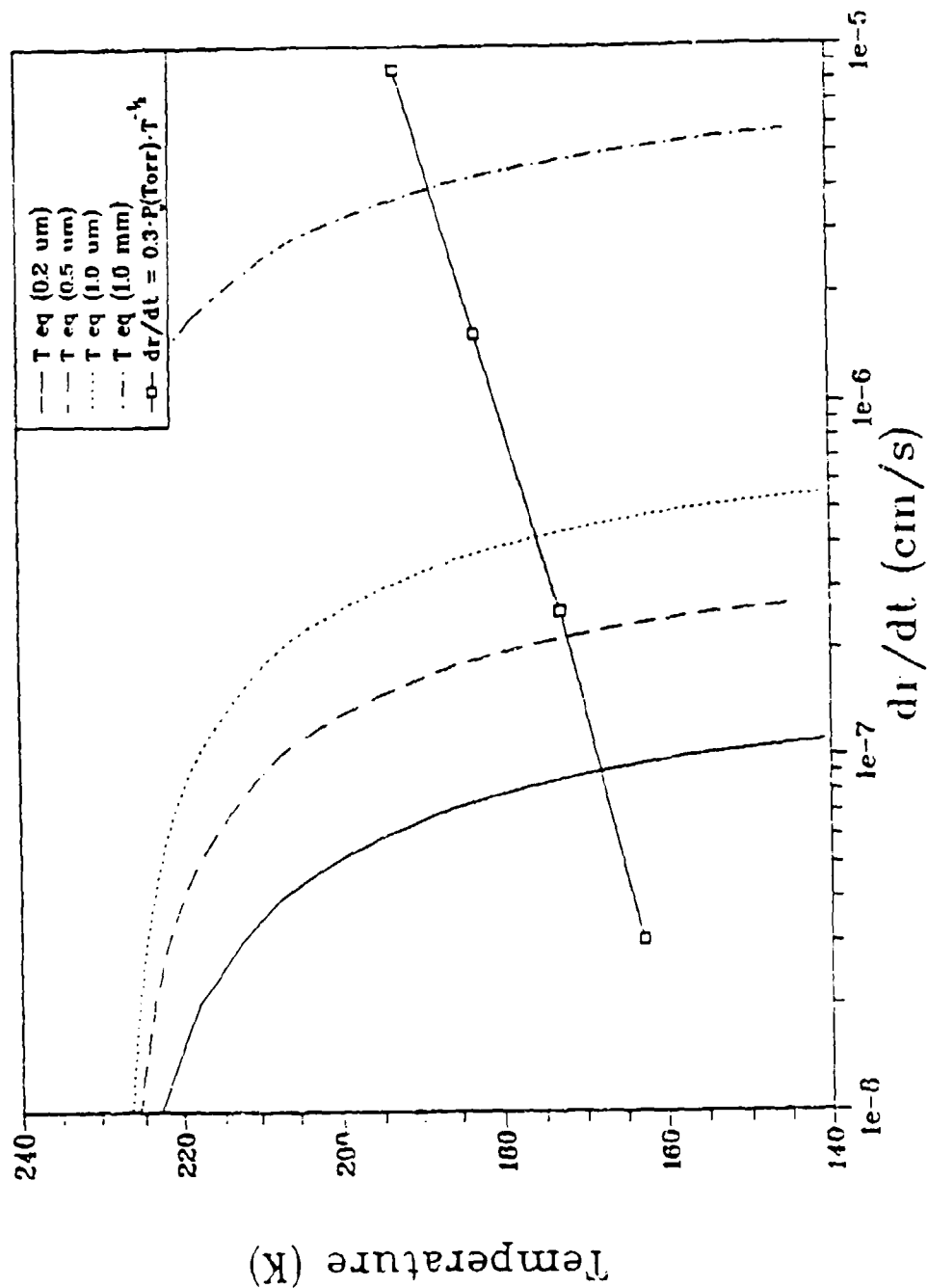


Figure B3. Graphical solution to equilibrium temperature of both small and large ice particles. The intersection of the vaporization rate ( $dr/dt$ ) with particle temperature derived from heat balance ( $dr/dt = 0$ ) is the equilibrium temperature.

in Equation (B5). The intersection of these curves is the asymptotic solution of Equation (B3).

A time scale for the approach to equilibrium can be established by equating the heat loss by sublimation to the heat gain from earthshine and sunlight (near equilibrium, the heat loss due to particle radiation is  $\sim 1/6$  of the total loss, and therefore is neglected for the purpose of this estimate); this takes place at about 0.6 seconds. (Surface roughening has a negligible effect on the cooling over this short period.) The asymptotic temperature is approached well before the small ice particles leave the region of image where blooming from Orbiter's sunlit body overwhelms the groundbased-video signals.

In summary, we have used Equations (B3) and (B5) to simultaneously solve the general rate Equation (B1) for  $T$  for all values of time. The submicron recondensation ice particles approach their thermodynamic equilibrium temperature of 166 K within about 1 second after they form.

## Appendix C

### TEMPERATURE HISTORY OF THE MILLIMETER-DIAMETER ICE PARTICLES

#### Introduction and Background

We calculate the temperature and decrease in size by evaporation/sublimation of the large--and as noted polydisperse--sunlit ice droplets in low earth orbit by a procedure similar to Appendix B, as input for our estimates in Appendix D of some of the infrared radiances of this particle cloud. In the interest of clarity and simplicity, we consider only a single ("mean") radius of assumed-spherical, non-fragmenting or -cracking particles, 0.13 cm.

These large explosion-product particles differ in emissivity from the small recondensation ice particles, as to a good approximation they can be considered blackbodies at the infrared wavelengths where they absorb earthshine and radiate thermally; refer to Figure A1. Since  $\epsilon_e = \epsilon_p \approx 1$ , the reflection of IR earthshine off these ice particles is small compared with their thermal radiation; and since the particle temperature is less than that of the earth (as will be shown), the trail exhibits "negative contrast" when viewed in the nadir. We calculated the emissivity/absorptivity  $\epsilon_s$  averaged over the spectrum of sunlight to be 0.15, a figure that decrease slightly as the droplet diameter decreases (more on this point in the next subsection).

A second major difference between the two water/ice components is in the redistribution of heat in the interior of the particles, which (as we will also find) takes place in the large droplets by conduction in times long compared with the characteristic times for sublimative-evaporative cooling of the droplet surfaces. That is, in these large particles the time step for cooling by sublimation--the dominant factor in the early cooling stages, as we saw in Appendix B--is controlled by diffusion of heat from the bulk to the exposed surface. The fact that the temperature varies with distance from the droplet center introduces an element of uncertainty in the sterances of these

particles, since their outermost "shell" is not opaque at all wavelengths (as is shown by the top set of plots in Figure A1).

A recent theoretical treatment of the initial cooling of coherent cylindrical liquid streams (Ref 4) provides a useful basis for estimating the time dependence of the temperature at the surface and in the interior of spherical water-ice droplets. This review also identifies conceptual difficulties and discrepancies between theory and observation, which underscore the unreliability of calculations of these temperatures over the few seconds during which the large ice droplets approach a heat-balance equilibrium analogous to that of the small droplets derived in Appendixes B and A. This situation is somewhat unfortunate in view of the obvious importance of the optical signature of the vented-water volume near the spacecraft (i.e., sensor platform) itself.

#### Qualitative Cooling Issues

We estimate the initial temperature of the water-as-droplets from the observed time before the explosion takes place, the rates of evaporative cooling of the coherent stream's surface during this time as calculated in Ref 4, and the thickness of this cooled outer liquid layer derived from heat-diffusion theory. (To repeat: we ignore the cracking and other irregularity development that results from the expansion of water as it freezes.) The time of flight to the about 1/2-m distance from the venting nozzle where the video camera on the Remote Manipulator Arm shows a bundled supply water stream breaking up is  $\sim 2 \times 10^{-2}$  s. During this brief period the surface temperature of the column falls from its adopted initial 333K--the nominal nozzle temperature--to about 250K (see Figure 4 of Ref 4).

The radial thickness of this annular heat "diffusion layer" is  $[(4/\pi) \cdot (\text{diffusivity of 300K water}) \cdot 2 \times 10^{-2} \text{ s}]^{1/2}$ ; we take the diffusivity  $K' [\equiv (\text{thermal conductivity})/(\text{density}) \cdot (\text{specific heat})]$  to be its handbook value,  $0.00144 \text{ cm}^2/\text{s}$ . The resulting shell thickness is 0.06 mm, which is very closely 1/10 of the

relaxed-stream radius calculated in Section 7. (Conduction and the convective mixing accompanying the cavitation explosion would momentarily prevent ice from forming in the droplets.) Thus a mean temperature of the water droplets produced by the rupturing the stream would be  $333\text{K} - (2 \times 0.1 \times [(333 - 250)/2])\text{K} \approx 325\text{K}$ . The fraction of vented water evaporated in this pre-breakup period--that is, the fraction that reduces the mean temperature of the liquid quasicylinder by  $8^\circ\text{C}$ , with the heat of vaporization taken as the  $560\text{ cal/gm}$  shown in Figure B1--is 0.014. This fraction is about  $1/20$  of the total water that vaporizes/sublimes.

The "phases" in cooling of these assumed-spherical water particles would afterwards be as follows. In practice, the particles are not homogeneous or (in particular) isothermal, as is further explained in the next subsection where we estimate time scales of cooling; the arguments immediately below are intended principally to provide some physical insight into the cooling process and estimate the mass loss.

a) Evaporation of the initially  $325\text{K}$  liquid until its temperature falls to  $273\text{K}$ . Applying the  $580\text{ cal/gm}$  mean heat of vaporization from Figure B1, we find that the resulting fractional decrease in the radius of each (still assumed-spherical) droplet is 0.030, so that the radius is reduced from  $0.130$  to  $0.126\text{ cm}$ . (We carry three significant figures only to scope the magnitudes of the changes in particle radii at each step.)

b) Freezing at constant temperature, resulting in a further fractional decrease in radius of 0.04. (We neglect the small difference between the densities of solid and liquid water.) Adopting the mean handbook value of  $0.005\text{ cal}/(\text{cm}\cdot\text{s}\cdot^\circ\text{C})$  as its thermal conductivity we find that the heat diffusivity of pure ice is almost nine times that of liquid water near  $0^\circ\text{C}$ ; in consequence the characteristic heat penetration times become some nine times shorter after the particles solidify (neglecting advection in liquid water, a condition assumed in Ref 4).

c) Further decrease in temperature of the ice droplet, still principally by sublimation. Anticipating the equilibrium temperature to be calculated in the following subsection, we take 200K to be the temperature at which the radiation terms on the right side of Equation (B1) become comparable with the  $\dot{r}$  term. The further fractional decrease in radius of the drop over 73 C° is then 0.014, to 0.119 cm. The three above steps a), b), c) thus represent a total radius decrease of 8% up to this point, or one-quarter of the volume of the initially-liquid droplet (still neglecting the difference between the densities of liquid and solid water).

d) Asymptotic approach to the equilibrium daytime temperature. Since the sublimation rate is still decreasing (relative to the radiation rate as well as absolutely), the particle radius undergoes a negligible change during this (relatively long) period.

e) Equilibrium sublimation, at a rate of closely  $4 \times 10^{-6}$  cm/s as can be taken from Figure B3 and is re-derived below. Thus over the 120 seconds during which the large particles travel  $2\frac{1}{2}$  km--the length of the accompanying small-particle cloud responsible for the AMOS video exposures--these large particles lose only an additional 0.5% of their radius.

The total change in (mean) radius of these stream rupture-product particles, virtually all of which takes place within a few 10's m from the spacecraft, can be seen to be less than 10%. This finding justifies neglect of radius changes in 1) estimating from surface-brightness arguments the fraction of the vented water recondensed into small particles (as is done in Section 11), and 2) calculating the effective particle absorptivity/emissivity  $\epsilon_s$  averaged over the solar-irradiance spectrum.

### Energy Balance

As noted above, the mm-diameter ice particles are to a reasonable approximation blackbodies in the infrared, and their absorptivity/emissivity  $\epsilon_s$  weighted over the solar spectrum is

about 0.15. As the ratios of emissivities are roughly the same as those for the submicron ice particles (see Figure A1), the principal heating is again from infrared earthshine. Since their rate of heat absorption per unit area is higher (and independent of radius), the large ice particles would be expected to come to a higher equilibrium temperature than the small particles.

We have estimated the time dependence of the surface temperature of the large particles by iteratively solving the energy balance equation, taking into account the interior temperature gradients. Within the first second after the collimated stream fragments the loss of heat is effectively all from evaporation/sublimation; we equated this loss with a decrease in the temperature of an outer shell of the droplet whose thickness is determined by thermal diffusion in the liquid or solid. We approximated the thickness of this effectively cooled layer  $\Delta r$  in cooling time to be  $(K't)^{1/2}$ , where  $K'$  is the thermal diffusivity defined above. In practice, the flow of heat through this shell determines the time scale of cooling of the large water/ice particles.

Equating the loss and gain of heat, we get

$$(4\pi/3)(r^3 - [r - \Delta r]^3) \rho C_w \Delta T = (4\pi/3)(r^3 - [r - \dot{r}\Delta t]^3) \rho L, \quad (C1)$$

where the symbols are as defined in Appendix A and  $C_w$  is the specific heat of liquid water. Since the cooled layers are initially very thin compared with  $r$  this expression reduces to

$$\Delta r C_w \Delta T = \dot{r} \Delta t L, \quad (C2)$$

where  $\Delta t$  is the time step during which the layer temperature decreases by  $\Delta T$ . Equation (C2) is obviously valid only for the liquid, that is, in the range of surface temperatures between the initial droplet temperature (325K) and freezing (273K).

To model the energy balance when the surface starts to solidify, two further terms are added that take into account the

phase transition from liquid to solid in an immediately-inner shell and the cooling of the outer layer of ice:

$$\Delta r_w C_w \Delta T + H(K' \Delta t)^{\frac{1}{2}} + \Delta r_i C \Delta T = \dot{r} \Delta t L. \quad (C3)$$

Here  $\Delta r_w$  and  $\Delta r_i$  represent the thicknesses of these concentric liquid and solid shells, and  $H$  is the heat of fusion of water (which we took as 80 cal/gm). The first term on the left side of Equation (C3) recapitulates Equation (C2); the second term is the heat extracted when the inner shell freezes; and the third term represents the cooling of the solidified water layer (we continue to neglect the small difference between the densities of liquid water and ice).

We solved Equations (C2) and (C3) iteratively down to approximately 200K with temperature step  $\Delta T = 1 \text{ C}^\circ$ . Near 200K the thickness of the effectively-cooled layer reaches ~25% of the particle radius, and the radiative terms are becoming comparable with the sublimative cooling term. We therefore assumed homogeneous cooling of the large particles below 200K, and determined the time dependence of their surface (and bulk) temperature by the same procedure used for the small, isothermal ice particles in Appendix B.

### Conclusion

The resulting time dependence of outermost-surface temperature of the droplets is shown in Figure C1. 200K is reached in about 10 s, at which time the particles have moved some 200 m from the venting nozzle. The large particles then approach their asymptotic temperature of 180K in the remaining ~100 s of their path during which the accompanying cloud of sunlight-scattering small particles remains above the threshold of the long focal length, low light level video camera system at AMOS.

This equilibrium temperature is predicted by the calculational approach outlined in Appendix B, as the



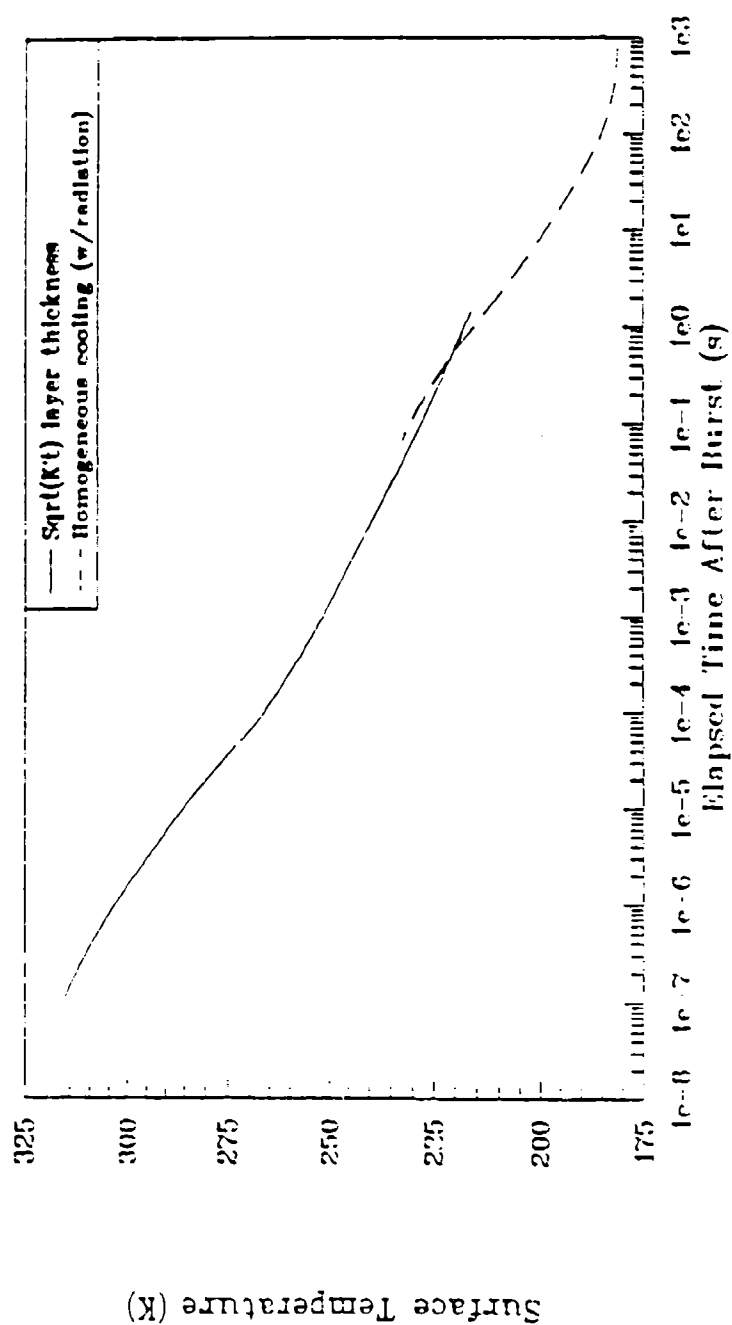


Figure C1. Surface temperature history of the -mm ice particles. Outer shell cooling is calculated for the first second after burst (solid line), bulk particle cooling is applied after that time (dashed line).

intersection of the evaporation rate of Equation (B5) and the plot of energy gain/loss rate due to radiation by 1-mm ice spheres. (This latter quantity is virtually independent of radius when the particle is a black body in the infrared.) As expected, the final temperature of the large particles is somewhat higher than that of the lower-absorptivity/emissivity submicron ice particles.

## Appendix D

### INFRARED RADIATION FROM THE WATER TRAIL

#### Scope

We review very briefly here the emission and scattering from the vented water at wavelengths outside the S-20R (essentially, visible) spectrum range to which the video cameras at AMOS and onboard space shuttle respond.

An overview of the physical and radiative properties of the three components of the trail--including the unrecondensed water vapor, not otherwise explicitly considered in this report--appears in Table D1, and some estimates of infrared thermal radiances of the large-particle cloud viewed perpendicular to its symmetry axis close to and 1 km from the spacecraft are in Table D2. Radiant intensities at further aspect angles and longitudinal intercept distances, and in other spectrum intervals, can be straightforwardly derived from

- the particle emissivities (/reflectivities) and scattering cross-sections in Figures 9 and A1,
- the particle temperatures in Figure C1 (and B2),
- the spectral irradiances from sunlight and earthshine, and
- the trail dimensions and particle concentrations derived in the main text (which were applied to estimate the absolute visible brightnesses resulting from scattering of direct sunlight).

The thermal radiances in the atmosphere's medium- and long-wavelength infrared "windows" in Table D2 are intended only to be representative of the many possible combinations of wavelength response and view projection of surveillance sensors.

#### Discussion

The brightness of the optically-thin cloud in general varies with  $(X \sin \eta_2)^{-1}$ , the product of sight path through it and particle density ( $\sim 1/X^2$ ) within it. (Angle  $\eta_2$  is defined in Figure 3b.) The dependence of radiance on wavelength follows

Table D1. Radiation from the Water Trail at Other Than Visible Wavelengths

Water Component	Fraction	Spatial Distribution	Temperature	UV Radiation	SWIR* Radiation	LWIR** Radiation
Large Ice Particles	0.8	As Figures 1 and 7; $\chi^2$ in cone	Figure C1; eventually 180K	Sunlight scatter, geometric	(~1; negligible scatter, weak thermal	Negligible scatter, some thermal
Small Ice Particles	0.003	As Figures 2 and 4-5; $\chi^2$ in cone	Figure B2; eventually 166K	Sunlight scatter, near-Rayleigh	Weak scatter, very weak thermal	Very weak scatter and thermal
Unrecondensed Vapor	0.2	Not considered here	1000K after mixing with atmosphere	Molecular scatter, negligible	Earthshine & solar scatter 2.7 $\mu\text{m}$ $\nu_3$ - $\nu_1$	Earthshine scatter in 6.3 $\mu\text{m}$ $\nu_2$

\* 3-5  $\mu\text{m}$

\*\* 8-13  $\mu\text{m}$  Infrared Window

--Considerable impact excitation--  
--Also rotational lines--

Table D2. Infrared Radiances of Thermal Emission Viewing Perpendicular to the Axis of the Large-Particle Trail

Band	$X = 1000 \text{ m}$ $\epsilon' = 10^{-6}$		$X = 1 \text{ m}$ $\epsilon' = 10^{-3}$	
	$T = 190\text{K}$		$T = 260\text{K}$	$T = 325\text{K}$
3-5 $\mu\text{m}$	$1.3 \times 10^{-13}$ *		$1.1 \times 10^{-8}$	$1.4 \times 10^{-7}$ w/sr-cm <sup>2</sup>
8-12 $\mu\text{m}$	$7.6 \times 10^{-11}$		$5.7 \times 10^{-7}$	$1.8 \times 10^{-6}$ w/sr-cm <sup>2</sup>
at 10 $\mu\text{m}$	$1.9 \times 10^{-13}$		$1.5 \times 10^{-12}$	$1.5 \times 10^{-9}$ w/sr-cm <sup>2</sup> -cm <sup>-1</sup>

\*Plus scattered sunlight; see text.

standard Rayleigh-Mie theory for self-emission and scattering of infrared earthshine and both direct and atmosphere-scattered sunlight/moonlight.

The solar-scatter intensities are weak at ultraviolet wavelengths (fifth column in Table D1) due to the rapid decrease in the spectral irradiance of sunlight below  $0.4 \mu\text{m}$ . Since the large ice particles have emissivity near 1 in the long-wavelength infrared (Figure A1), they reflect little earthshine. The submicron particles radiate and scatter increasingly less radiation as the ratio  $2\pi r/\lambda$  decreases, with the result that the infrared brightnesses from this component of the water trail--which as we have seen dominate the solar scattering to AMOS--are very small compared with the infrared brightnesses of the mm-diameter ice particles.

We have included for completeness of Table D1 the unrecondensed water vapor, whose collisionally and optically excited radiations are not detected by the video cameras (and so extend beyond the scope of this report). Unlike the ice particles, this gas loses kinetic energy by colliding with the residual atmosphere. The  $\text{H}_2\text{O}$  molecules would radiate both their familiar  $\nu_1\nu_2\nu_3$  vibrational-band sequences (see for example Ref 13) and spectrally-widespread rotational lines. In addition, short-wavelength infrared (and some visible) radiation would be expected from ventings of water (Ref 14), from excitative interchange reactions of gaseous  $\text{H}_2\text{O}$  with ambient O that produce vibrationally-excited OH. (About the fourth vibrational state of hydroxyl is energetically accessible when the velocity of  $\text{H}_2\text{O}$  relative to the atmosphere is  $7\text{-}3\frac{3}{4} \text{ km/s}$ .)

The infrared radiances in Table D2 from the large (assumed-spherical and -monodisperse) particles were calculated as the Planck radiation by a dilute array of black bodies at the temperatures derived in Appendix C. The emissivities  $\epsilon'$  listed represent the fractional area covered by this cloud of droplets in the projections perpendicular to its velocity (that is, to the spacecraft's trajectory). We have listed radiances at two

temperatures for the water-ice trail at 1 m from the venting nozzle, insofar as at this early time after their formation the temperature at the surface of the large particles is much lower than that in their interior and their outermost shell(s) would not be optically thick; the actual radiances would lie between these extremes. (Further error is introduced here by our approximating the density of ice as that of liquid water, and of course by considering the particles to be spherical.) The tabulated radiance values for the 3 to 5  $\mu\text{m}$  wavelength interval do not take into account scattering of sunlight, which despite the low reflectivity of the large ice droplets would be at least comparable to their thermal radiation when their temperature falls to its asymptotic value 185K.

Since the effective temperature of these large droplets at longitudinal distances  $X > 10$  m is in general less than the radiating temperature of the earth and atmosphere, the water trail would exhibit "negative contrast" in nadir projections; that is, its brightness would be less than that of the lower-atmospheric and hard-earth background. On the other hand the spectral radiance of the trail at 11  $\mu\text{m}$  (within the long wavelength-infrared "window"),  $2 \times 10^{-13}$  and  $\sim 3 \times 10^{-9}$   $\text{w/cm}^2 \text{ sr cm}^{-1}$  at  $X = 1$  km and 1 m respectively, is large compared with that of the atmosphere's limb calculated by the "AFGL" radiation model (Ref 19):  $10^{-15}$   $\text{w/cm}^2 \text{ sr cm}^{-1}$  at 200 km tangent intercept altitude, increasing to  $10^{-14}$   $\text{w/cm}^2 \text{ sr cm}^{-1}$  at 120 km. Even in the adjacent strong  $\nu_3$  emission band of ozone centered at 9.6  $\mu\text{m}$  the limb spectral radiance becomes as high as  $10^{-9}$   $\text{w/cm}^2 \text{ sr cm}^{-1}$  only at altitudes as low as 90 km. These figures indicate that the radiances of the water-particle trail viewed in limb and zenith projections substantially exceed those of the atmosphere (although perhaps not the celestial background) in the LWIR window wavelength region.

## REFERENCES

1. E. Murad, Implications of mass spectrometer measurements on space shuttle, Planet. Space Sci. 33, 421-423, 1985.
2. J. S. Pickett, N. D'Angelo, and W. S. Kurth, Plasma density fluctuations observed during Space Shuttle Orbiter water releases, J. Geophys. Res. 94, 12081-12086, 1989.
3. P. A. Bernhardt, A critical comparison of ionospheric depletion chemicals, J. Geophys. Res. 92, 4617-4628, 1987.
4. E. P. Muntz and M. Orme, Characteristics, control, and uses of liquid streams in space, AIAA J. 25, 746-756, 1987.
5. M. E. Fowler, L. J. Leger, M. E. Donahoo, and P. D. Maley, Contamination of spacecraft by recontact of dumped liquids, Third Annual Space Operations, Automation, and Robotics Symposium (SOAR 89), NASA Conf. Pub. 3059, pp. 99-104, 1989.
6. T. T. Kassal, Scattering properties of ice particles formed by release of H<sub>2</sub>O in vacuum, J. Spacecraft Rockets 11, 54-56, 1974.
7. H. Fuchs and H. Legge, Flow of a water jet into vacuum, Acta Astronautica 6, 1213-1226, 1979.
8. B. P. Curry, R. J. Bryson, B. L. Seibner, and J. H. Jones, Selected Results from an Experiment on Venting an H<sub>2</sub>O Jet into a High Vacuum, Arnold Engineering Development Center Technical Report AEDC-TR-84-28, Jan 1985.
9. B. P. Curry, R. J. Bryson, B. L. Seibner, and E. L. Kiech, Additional Results from an Experiment Venting an H<sub>2</sub>O Jet into a High Vacuum, Arnold Engineering Development Center Technical Report AEDC-TR-85-3, Jun 1985.
10. Avco Research Laboratory (Everett, MA), AMOS Users' Manual, Unnumbered-undated, 94 + 31 pp.
11. L. A. Freedman, The space shuttle closed circuit television system, Proc. IEEE 1981 National Aerospace and Electronics Conference, pp. 23-30, May 1981.
12. H. Patashnick and G. Rupprecht, Sublimation of Ice Particles in Space, Martin-Marietta Technical Report ED-2002-1654, March 1973.

13. D. G. Koch, G. G. Fazio, W. Hoffmann, G. Melnick, G. Reike, J. Simpson, F. Witteborn, and E. Young, Infrared observations of contaminants from Shuttle flight 51-F, Adv. Space Res. 7, No. 5, 211-219, 1987.
14. I. L. Kofsky, J. L. Barrett, T. E. Brownrigg, P. J. McNicholl, N. H. Tran, and C. A. Trowbridge, Excitation and Diagnostics of Optical Contamination in the Spacecraft Environment, AFGL-TR-88-0293, ADA202429, 01 Jul 1988.
15. I. L. Kofsky, N. H. Tran, M. A. Maris, and C. A. Trowbridge, Measurement of Optical Radiations in the Spacecraft Environment, GL-TR-89-0168, ADA213814, 15 June 1989.
16. R. D. Sharma and C. Buffalano, Temperature and size histories of liquid H<sub>2</sub>, O<sub>2</sub>, and H<sub>2</sub>O particles released in space, J. Geophys. Res. 76, 232-237, 1971.
17. A. Berk, private communication, 1989.
18. C. F. Bohren and D. R. Huffman, Absorption and Scattering of Light by Small Particles, Wiley, New York, 1983.
19. T. C. Degges and H. J. P. Smith, A High Altitude Infrared Radiance Model, AFGL-TR-77-0271, ADA059242, 30 Nov 1977.
20. C. P. Pike, D. J. Knecht, R. A. Viereck, E. Murad, I. L. Kofsky, M. A. Maris, N. H. Tran, G. Ashley, L. Twist, M. E. Gersh, J. B. Elgin, A. Berk, A. T. Stair, Jr., J. P. Bagian, and J. F. Buchli, Release of liquid water from the space shuttle, Geophys. Res. Lett. 17, 139-142, 1990.
21. R. A. Viereck, E. Murad, C. P. Pike, I. L. Kofsky, C. A. Trowbridge, D. L. A. Rall, A. Setayesh, A. Berk, and J. B. Elgin, Photometric Analysis of a Space Shuttle Water Venting, Paper E 3-1 at the Fourth Annual Space Operations, Applications, and Research Symposium, Albuquerque, 26-28 June 1990.